# KECK SPECTROSCOPY OF FAINT $3 < z < 7$ LYMAN BREAK GALAXIES. III. THE MEAN ULTRAVIOLET SPECTRUM AT $z \simeq 4$

TUCKER JONES[1], DANIEL P. STARK[2,3,4], AND RICHARD S. ELLIS[1]

[1] Astronomy Department, California Institute of Technology, MC249-17, Pasadena, CA 91125, USA
[2] Institute of Astronomy, Cambridge CB3 0HA, UK
[3] Steward Observatory, University of Arizona, Tucson, AZ 85721, USA

## ABSTRACT

We present and discuss the mean rest-frame ultraviolet spectrum for a sample of 81 Lyman break galaxies (LBGs) selected to be $B$-band dropouts at $z \simeq 4$. The sample is mostly drawn from our ongoing Keck/DEIMOS survey in the GOODS fields and augmented with archival Very Large Telescope data. In general, we find similar spectroscopic trends to those found in earlier surveys of LBGs at $z = 3$. Specifically, low-ionization absorption lines which trace neutral outflowing gas are weaker in galaxies with stronger Ly$\alpha$ emission, bluer UV spectral slopes, lower stellar masses, lower UV luminosities, and smaller half-light radii. This is consistent with a physical picture whereby star formation drives outflows of neutral gas which scatter Ly$\alpha$ and produce strong low-ionization absorption lines, while increasing galaxy stellar mass, size, metallicity, and dust content. Typical galaxies are thus expected to have stronger Ly$\alpha$ emission and weaker low-ionization absorption at earlier times, and we indeed find somewhat weaker low-ionization absorption at higher redshifts. In conjunction with earlier results from our survey, we argue that the reduced low-ionization absorption is likely caused by lower covering fraction and/or velocity range of outflowing neutral gas at earlier epochs. Although low-ionization absorption decreases at higher redshift, fine-structure emission lines are stronger, suggesting a greater concentration of neutral gas at small galactocentric radius ($\lesssim 5$ kpc). Our continuing survey will enable us to extend these diagnostics more reliably to higher redshift and determine the implications for the escape fraction of ionizing photons which governs the role of early galaxies in cosmic reionization.

*Key words:* galaxies: evolution – galaxies: high-redshift – galaxies: ISM

*Online-only material:* color figures

## 1. INTRODUCTION

Considerable progress has been made over the past decade in charting the demographics of high-redshift galaxies. Multi-wavelength surveys have defined the luminosity functions of UV and submillimeter selected star-forming sources (Reddy & Steidel 2009; Wardlow et al. 2011) as well as the coeval population of quiescent massive red galaxies (Brammer et al. 2011). *Spitzer* data have revealed the time-dependent *stellar mass density*—a complementary quantity which represents the integral of the past star formation activity (e.g., Stark et al. 2009). Through these surveys, a well-defined picture of the history of star formation and mass assembly over $0 < z < 6$ has been empirically determined (Hopkins & Beacom 2006; Ellis 2008; Robertson et al. 2010). The redshift range $2 < z < 3$ corresponds to the peak of star formation activity where the Hubble sequence starts to emerge, and the earlier era corresponding to $3.5 < z < 5$ is an even more formative one where mass assembly was particularly rapid.

Intermediate dispersion spectroscopy of carefully selected Lyman break galaxies (LBGs) has been particularly important in defining population trends that cannot be identified from photometric data alone. A very influential study at $z \simeq 3$ was undertaken by Shapley et al. (2003), who used composite Keck LRIS spectra of various subsets of nearly 1000 LBGs to examine the role of hot stars, H II regions, and dust obscuration, as well as to measure the outflow kinematics and absorption line properties of neutral and ionized gas. Composite spectra are particularly useful for measuring weak lines which cannot be studied in

detail for individual objects. Through these careful studies, a detailed picture of the mass-dependent evolution of LBGs has emerged (see Shapley 2011 for a recent review).

In earlier papers in this series (Stark et al. 2010, hereafter Paper I; Stark et al. 2011, hereafter Paper II), we introduced an equivalent spectroscopic survey of LBGs selected from a photometric catalog of more distant LBGs with $3 < z < 7$ in the Great Observatories Origins Deep Survey (GOODS) fields (Giavalisco et al. 2004; Stark et al. 2009). Whereas the Shapley et al. (2003) study targeted the study of LBGs close to the peak of activity in the overall cosmic star formation history, this earlier period corresponds to a less well-studied era when the rate of mass assembly is particularly rapid. From photometric data alone, Stark et al. (2009) deduced some significant changes in the characteristics of star formation at $z \simeq 4$–6 compared to later times, for example, a shorter timescale of activity ($\simeq 300$ Myr). We considered it crucial to understand these changes in LBG properties if these galaxies are to be used as probes of cosmic reionization at higher redshifts.

At the time of writing, our Keck survey is continuing with increasing emphasis at high redshift. Paper I presented the first substantial results from a survey of LBGs at $3.5 < z < 6$ observed with the Keck/DEIMOS spectrograph. Paper II augmented this data with a further sample following more ambitious exposures focusing primarily on $z \simeq 6$ LBGs. Incorporating a sample of ESO Very Large Telescope (VLT) spectra, retrospectively selected using similar photometric criteria as those for the Keck sample from the FORS2 study of Vanzella et al. (2005, 2006, 2008, 2009), the current data set amounts to a sample of 546 galaxies over the redshift range $3.5 < z < 6.3$.

---

[4] Hubble Fellow.

Our earlier papers in this series concentrated primarily on the rate of occurrence of Lyman $\alpha$ (Ly$\alpha$) emission in our spectra (the "Ly$\alpha$ fraction"). The overall goal was to understand the significantly different evolutionary trends in the luminosity functions of LBGs and narrowband-selected Ly$\alpha$ emitters (LAEs; Ouchi et al. 2008) prior to the use of the Ly$\alpha$ fraction as a test of when reionization ended (Schenker et al. 2012). Paper I confirmed a result found by Shapley et al. (2003) at lower redshift, namely that Ly$\alpha$ emission is more frequent in lower luminosity LBGs rising to a high proportion $\simeq 50\%$ at $M_{UV} = -19$. More importantly, the Ly$\alpha$ fraction was found to rise modestly with redshift over $3 < z < 6$. By correlating the visibility of Ly$\alpha$ emission with UV continuum slopes derived from the *Hubble Space Telescope* (*HST*) photometry, it was argued that these trends in the visibility of line emission most probably arise from different amounts of dust obscuration. Reduced dust extinction in lower luminosity LBGs and those at higher redshift has also been deduced from studies of larger photometric samples (Bouwens et al. 2009; see also Reddy & Steidel 2009).

Paper I also discussed the possibility that the covering fraction of hydrogen may be lower in low-luminosity LBGs. Strong Ly$\alpha$ emission in luminous LBGs is often associated with low equivalent width interstellar absorption lines arising from a non-uniform covering fraction of neutral hydrogen (Quider et al. 2009; Shapley et al. 2003). This trend suggests that the high Ly$\alpha$ fraction in faint LBGs is partially due to a lower covering fraction, which would imply that Lyman continuum photons may more easily escape from intrinsically faint $z \simeq$ 4–6 galaxies. Such a result would have great importance in understanding the role of $z > 7$ galaxies in maintaining cosmic reionization (Robertson et al. 2010).

The present paper represents our first analysis of the spectral properties of $z \simeq$ 4–5 LBGs derived from composite spectra in the manner pioneered at $z \simeq 3$ by Shapley et al. (2003). The large database now amassed following the campaigns at Keck and the VLT makes a similar study now practical in the redshift range where there is evidence of increased short-term star formation and the mass assembly rate is particularly rapid. Via detailed studies of low-ionization absorption line and emission line profiles, we aim to examine possible changes in the kinematics and covering fraction of neutral gas, which affects the strength of Ly$\alpha$ and the escape fraction of ionizing photons, as we approach the reionization era. As our redshift survey continues, in this paper we focus on a sample of galaxies with $3.5 < z < 4.5$, selected as $B$-dropout LBGs. Combining our Keck sample with data from the VLT (see Paper I for details), herein we examine the spectral features and trends in composite spectra drawn from a sample of 131 galaxies.

The plan of the paper is as follows. We briefly review the spectroscopic observations and their data reduction in Section 2; much of the relevant discussion is contained in Paper I. In Section 3, we describe the selection of individual spectra that we consider appropriate for forming the composite mean spectrum at $z \simeq 4$ and the associated sources of uncertainty. Section 4 examines the mean spectrum in detail and introduces the various diagnostic features in the context of a physical model for LBGs of different masses and star-formation rates. In Section 5, we compare spectroscopic trends grouped by observable properties such as mass and luminosity with those found at $z \simeq 3$ by Shapley et al. (2003). In Section 6, we discuss those trends which appear to be redshift-dependent, discussing implications for the role of early star-forming galaxies in

cosmic reionization. Finally, we summarize our results in Section 7.

Throughout this paper, we adopt a flat $\Lambda$CDM cosmology with $\Omega_\Lambda = 0.7$, $\Omega_M = 0.3$, and $H_0 = 70\ h_{70}$ km s$^{-1}$ Mpc$^{-1}$. All magnitudes in this paper are quoted in the AB system (Oke 1974).

## 2. OBSERVATIONS AND DATA REDUCTION

The rationale and procedures used to undertake our spectroscopic survey of LBGs over $3 < z < 7$ were introduced in detail in Paper I and the interested reader is referred to that paper for further detail. Here, we recount only the basic details. Our target LBGs were selected as $B$-, $V$-, or $i'$-band "dropouts" based on deep photometry in the two GOODS fields. The photometric catalog used in our analysis will be described in detail in D. P. Stark et al. (2012, in preparation). The selection and photometric approach is largely similar to that described in Stark et al. (2009) and Paper I, but we highlight two key updates. First, the selection is performed on the v2 GOODS ACS catalogs. Second, we utilize deep ground-based near-IR imaging in GOODS-N obtained from WIRCAM on Canada–France–Hawaii Telescope (Wang et al. 2010) and deep *HST* Wide Field Camera 3/IR imaging of GOODS-S from CANDELS (Grogin et al. 2011; Koekemoer et al. 2011).

### 2.1. Keck/DEIMOS

The majority of spectra we present are taken from an ongoing survey with the DEep Imaging Multi-Object Spectrograph (DEIMOS; Faber et al. 2003) on the Keck II telescope. In this paper, we have used observations taken in 2008 April and 2009 March (masks GN081, GN082, GN083, GN094, and GN095 in Paper I), which targeted a total of 261 $B$-drop and 88 $V$-drop galaxies. These data were taken with the 600 lines mm$^{-1}$ grating, covering the wavelength range 4850–10150 Å with a resolution of $\simeq$3.5 Å. We do not use data at wavelengths $\lambda > 9200$ Å which are affected by strong and variable absorption by atmospheric water vapor. The seeing was typically $0\rlap.''8$ and ranged between $0\rlap.''5$ and $1\rlap.''0$ during the observations.

All data were reduced and calibrated using a modified version of the IDL pipeline SPEC2D, developed specifically for DEIMOS by the DEEP2 survey team (Davis et al. 2003). The data were reduced as described in Paper I, with the addition of two important modifications. First, the continuum traces of all target galaxies and other objects occupying the same slit were carefully masked to exclude object flux from the sky background model. Second, the b-spline fit to the sky background was modified to include a second-order polynomial fit to the spatial dimension. These modifications significantly improved the sky subtraction, particularly at long wavelengths $\lambda > 7000$ Å where bright sky lines can be problematic.

The reduced one- and two-dimensional spectra were visually inspected using the IDL program SPECPRO (Masters & Capak 2011). Spectra which suffered from poor data quality were excluded from further analysis. The exclusions included unacceptable amounts of scattered light within the detector mosaic, defective CCD columns, contamination from bright nearby sources, or poor sky subtraction, for example, arising from the location of the slit on the detector. A few low-redshift interlopers were also identified and excluded from further analysis. For the remaining spectra, redshifts were measured from either Ly$\alpha$ emission (where present) or interstellar absorption lines. Galaxies identified as hosting strong active galactic nuclei

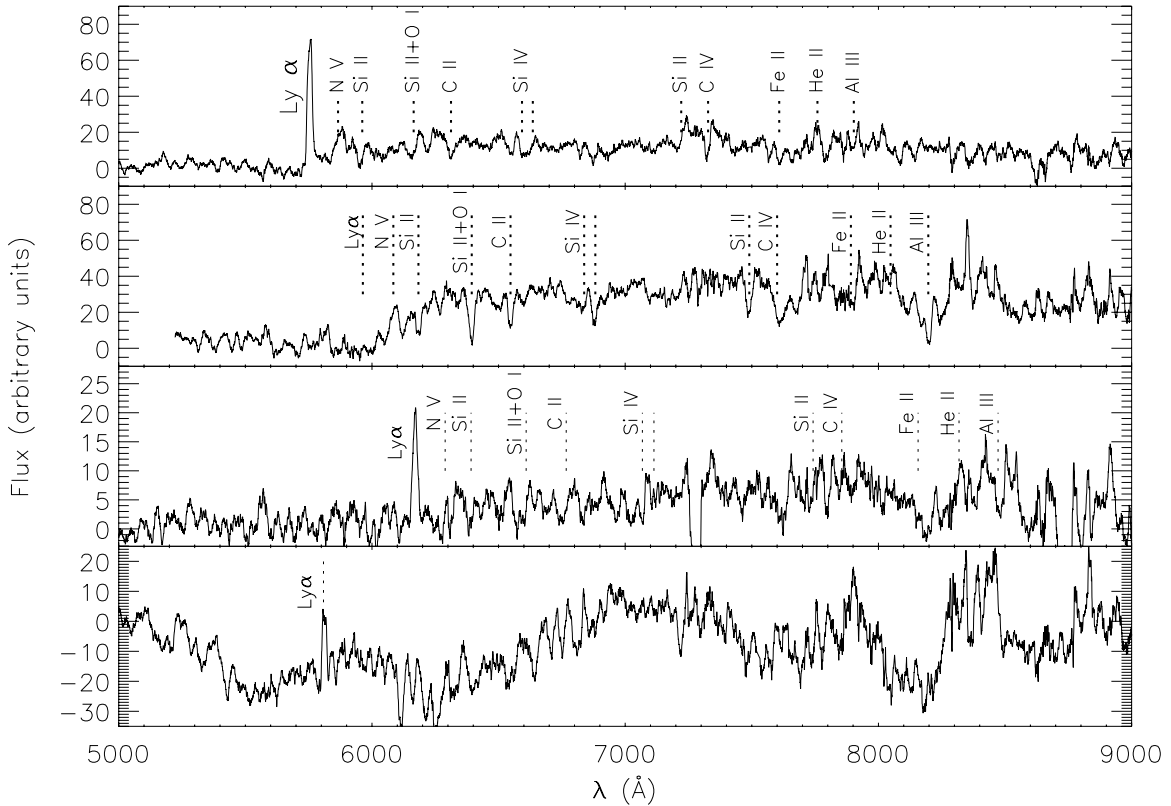**Figure 1.** Examples of individual DEIMOS spectra for $3.5 < z < 4.5$ LBGs. From top to bottom: a galaxy at $z = 3.73$ with Ly$\alpha$ emission and weak interstellar absorption features, a galaxy at $z = 3.906$ with Ly$\alpha$ and interstellar absorption, a faint galaxy at $z = 4.07$ with Ly$\alpha$ emission and no detectable absorption lines, and a galaxy at $z = 3.778$ with Ly$\alpha$ emission whose spectrum is contaminated by scattered light and detector defects. The top three spectra are included in stacking analyses while the bottom spectrum is excluded based on poor data quality. The continuum signal to noise in each spectrum degrades noticeably at wavelengths $\lambda > 7000$ Å due to increased OH sky emission.

(AGNs) based on the presence of C IV or other strong emission lines were excluded. We identified 5 stars, 2 dusty low-redshift galaxies ($z \sim 0.5$), 4 AGNs, and 134 star-forming galaxies with secure redshifts of $z > 3$. After rejecting poor data, the final sample consists of 94 high-quality spectra with accurate redshifts. Examples of high-redshift dropout spectra are shown in Figure 1.

### 2.2. Archival VLT/FORS2 Spectroscopy in GOODS-S

To augment our sample of high-redshift spectra, we have also made use of data from the FORS2 program of Vanzella et al. (2005, 2006, 2008, 2009) which targeted dropouts in the GOODS-S field. The characteristics of that survey in terms of resolution and spectral coverage are very similar to that undertaken at Keck with DEIMOS and details can be found in Paper I. Using the coordinates provided in the published FORS2 database, we queried the version 2.0 ACS catalogs for GOODS-S and undertook our own photometric measures and dropout selection criteria in an identical fashion to that used for our Keck survey. The magnitude distribution of the FORS2 sample is generally weighted toward sources brighter than those in the overall Keck survey, but for the purposes of constructing the mean spectra discussed in this paper, the bulk of the individual spectra are of comparable brightness.

### 2.3. Redshift Measurements

Care is needed in deriving accurate systemic redshifts from rest-frame UV spectra, since the strongest features trace the kinematics of outflowing gas rather than that of the stars. Stellar absorption lines are usually too faint to be measured precisely given the signal to noise of the spectra. Typically, the only features detected in individual spectra are Ly$\alpha$ and strong interstellar absorption lines such as Si II $\lambda1260$, O I $\lambda1302$+Si II $\lambda1304$, C II $\lambda1334$, Si IV $\lambda\lambda1393,1402$, Si II $\lambda1526$, and C IV $\lambda\lambda1548,1550$ (Figure 1). Absorption by outflowing gas results in a blueshift of interstellar absorption lines. Outflowing neutral hydrogen along the line of sight leads to an Ly$\alpha$ profile which displays very broad ($\gtrsim 1000$ km s$^{-1}$) blueshifted absorption and net redshifted emission. The high-ionization Si IV and C IV lines also arise in P-Cygni stellar winds with broad blueshifted absorption. The magnitude of these offsets has been well quantified for star-forming galaxies at $z \simeq 2.3$, and is typically $-200$ km s$^{-1}$ for interstellar absorption lines and $+500$ km s$^{-1}$ for Ly$\alpha$ emission (Steidel et al. 2010).

To determine accurate redshifts for making composite spectra, we restrict our sample to those with redshifts measured from either Ly$\alpha$ emission ($z_{\text{Ly}\alpha}$) or low-ionization interstellar absorption lines ($z_{\text{IS}}$). Although, as discussed above, these are not at the systemic redshift, we follow well-established techniques to correct for the typical offsets (Steidel et al. 2010). We do not use redshifts based on Ly$\alpha$ absorption or high-ionization lines (Si IV and C IV) because of the complex and variable blueshifts of these features with respect to the systemic redshift. We define $z_{\text{Ly}\alpha}$ as the centroid of the emission line and consider only spectra in which the line is detected at $>5\sigma$ significance. Interstellar absorption line redshifts require careful treatment to avoid spurious identification of sky line residuals. We consider only the low-ionization Si II $\lambda1260$, O I $\lambda1302$+Si II $\lambda1304$, and
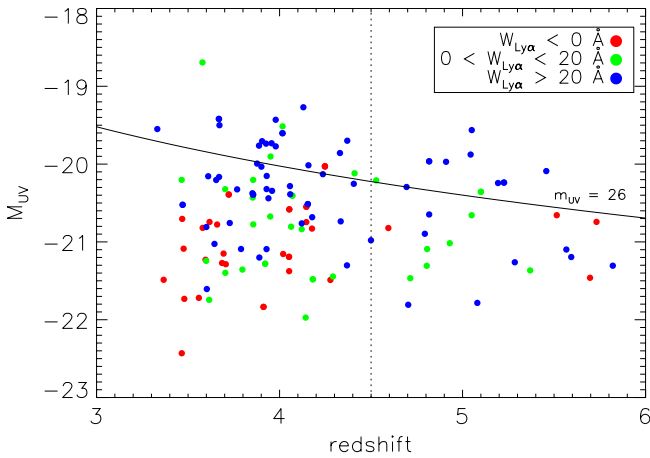
**Figure 2.** Redshifts and UV luminosities for the sample of 131 galaxies with suitably accurate redshifts measured either from Ly$\alpha$ or strong interstellar absorption lines. Points are color-coded according to the equivalent width of Ly$\alpha$, $W_{Ly\alpha}$. Galaxies brighter than an apparent magnitude $z'_{AB} < 26.0$ (solid line) typically have well-detected continua suitable for forming a composite spectrum. Galaxies with redshift $z < 4.5$ (dashed line) are used for the composite spectra discussed in Sections 3–5, while Section 6 includes galaxies at all redshifts shown here.

(A color version of this figure is available in the online journal.)

C $_{II} \lambda 1334$ features which are typically found in the highest signal-to-noise regions of our spectra. Absorption features at longer wavelengths are less reliable due to the higher density of strong night sky lines, while shorter wavelength transitions are lost in the Ly$\alpha$ forest. To measure absorption line redshifts, we first estimate the redshift from Ly$\alpha$ (either in emission or absorption). We then fit Gaussian profiles to the spectrum near the expected position of the three features above. We require the best fit of all three lines to be consistent to within $\pm 500$ km s$^{-1}$ with a combined significance of $>5\sigma$. If these conditions are met, then we define $z_{IS}$ as the weighted mean redshift of the three interstellar features.

With the criteria above, suitable redshifts are available for a total of 131 high-quality DEIMOS and FORS2 spectra. Ninety-one redshifts are based on measures of $z_{Ly\alpha}$ emission only, 31 have $z_{IS}$ only, and 9 have both $z_{Ly\alpha}$ and $z_{IS}$. The distribution of redshifts and absolute UV magnitudes for this sample is shown in Figure 2. Unless stated otherwise, further analysis in this paper is restricted to the 81 sources with redshift of $z < 4.5$ and apparent magnitude of $z'_{AB} < 26.0$. We applied this additional magnitude criterion in order to ensure a well-defined continuum signal/noise in each individual spectrum. Fifty-three of these 81 sources are drawn from the Keck survey and 28 from FORS2.

### 2.4. Sample Bias

While the sample is 90% complete for dropout-selected galaxies to an apparent magnitude of $z_{AB} = 25$, at fainter magnitudes Ly$\alpha$ emission or strong interstellar absorption features are required for reliable redshifts. This results in a bias toward stronger low-ionization absorption lines for the fraction ($\simeq 35\%$) without Ly$\alpha$. We can quantify this bias through the detectability of the average low-ionization absorption line strength shown in the composite spectrum in Figure 3 (see Section 3). We find that we can measure redshifts for this average absorption line strength with 90% completeness at $z_{AB} = 24.7$, declining through 50% at $z_{AB} = 25.2$ to zero at $z_{AB} > 25.5$. Of the galaxies with detected absorption line redshifts, those with $z_{AB} > 25.2$ have line strengths only 10% stronger than for those with $z_{AB} < 25.2$. Clearly this is a small effect.

The bias toward stronger Ly$\alpha$ emission for fainter galaxies is manifest in Figure 2 where a paucity of objects with $W_{Ly\alpha} < 20$ Å can be seen at faint magnitudes. This bias was fully quantified in Paper I using Monte Carlo simulations. For galaxies at $3.5 < z < 4.5$, a sample completeness of 95% is reached at $W_{Ly\alpha} \gtrsim 20$ Å for $z'_{AB} = 26$ and $W_{Ly\alpha} \gtrsim 7$ Å for $z'_{AB} = 25$. For the sample presented in this paper, the least biased subset is that with strong Ly$\alpha$ emission, followed by that with bright apparent magnitudes of $z'_{AB} < 25$.

A final issue in considering composite spectra is that these are comprised of individual spectra across $3.5 < z < 4.5$ with different rest-frame wavelength ranges. As our spectra generally cover the wavelength range 5000 Å $< \lambda <$ 9200 Å, galaxies at $z = 3.5$ contribute to the rest frame 1100–2050 Å, while those at $z = 4.5$ contribute to 900–1650 Å. At longer rest-frame wavelengths, the composite spectrum is therefore largely contributed by galaxies at lower redshift. In addition, there are wavelength-dependent sources of noise discussed in Section 3.2. In summary, the data used to construct the composite spectrum in Figure 3 correspond to a mean redshift $z = 3.98$ at $\lambda_{rest} = 1100$ Å, $z = 3.95$ at 1200 Å, $z = 3.90$ at 1500 Å, and $z = 3.82$ at 1650 Å. For the wavelength range of interest in this work, the redshift bias $\Delta z < 0.15$ is not particularly troublesome.

### 3. COMPOSITE SPECTRA

We now turn to the presentation of the composite spectra. We need to account for the difference between the redshifts determined using Ly$\alpha$ on the one hand and the low-ionization interstellar lines on the other hand and the systemic redshift prior to co-addition. We also seek to understand the signal/noise of the composite in terms of the statistical uncertainties and the variance among the individual spectra used to construct the composite.

Composite spectra are constructed by shifting the individual spectra into the rest frame according to a deduced systemic redshift and then averaging the set. In general terms, we will first identify a subsample based on their observable properties. Each spectrum in the sample is shifted to the adopted rest frame and interpolated to a common wavelength scale with a dispersion of 0.12 Å. All spectra are normalized to have a median of $f_\nu = 1$ in the range 1250–1500 Å. Spectra taken with DEIMOS are smoothed to a resolution of 1.9 Å to match the lower resolution of FORS2 data. The spectra are then averaged at each wavelength using a $\sigma$-clipped mean to reject outliers arising from sky subtraction residuals and cosmetic defects. An equal number of positive and negative outliers are rejected at each wavelength, totaling at most 30% of the data. The remaining data are averaged with an arithmetic mean.

Uncertainty in a composite spectrum will arise from both the finite signal to noise and the variance of the individual galaxies. For example, the variance in Ly$\alpha$ equivalent widths in our sample is much greater than the uncertainty measured in the individual spectra. It is especially important to quantify the sample variance for weak features that are generally not detected in individual spectra. We account for sample variance with a bootstrap technique. For each composite spectrum, we create 100 alternate composites using the same number of spectra but drawn at random from the parent sample. Each alternate has an average 63% of the sample represented with 37% duplicates. Every measurement made on the composite spectrum is repeated for each of the 100 alternates. We then take the measurement error to be the standard deviation of the
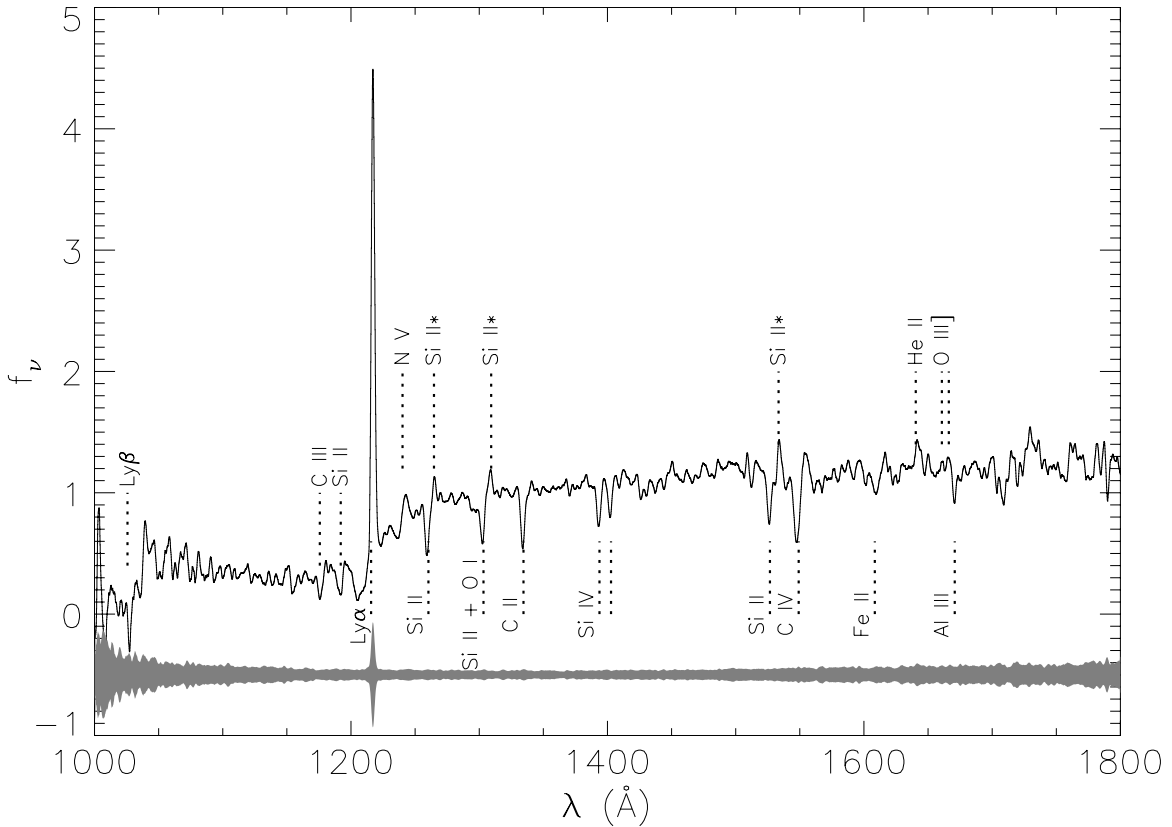
**Figure 3.** Composite spectrum of 81 galaxies in our sample with $3.5 < z < 4.5$ and apparent magnitude $z'_{AB} < 26$. The effective mean redshift for the sample averaged over wavelength is $\bar{z} = 3.9$. The strongest spectral features are labeled. The gray filled region shows the $\pm 1\sigma$ error at each point, determined from the scatter of individual spectra used to create the composite. The error spectrum peak at 1216 Å is due to large scatter in the intrinsic distribution of Ly$\alpha$ equivalent widths. The error is lowest at $\sim$1300–1500 Å where the continuum signal-to-noise ratio is $\simeq$30. The error increases at shorter wavelengths where the instrument throughput is lower and at longer wavelengths where sky emission is much stronger.

100 alternate measurements, which reflects both the sample variance and finite signal to noise.

As discussed in Section 2.3, the most challenging issue is to determine the systemic redshift prior to shifting to the rest frame. Here, we follow the approach used by Shapley et al. (2003). As a first approximation we use the value of $z_{Ly\alpha}$ (where available) to construct a composite spectrum. This enables us to locate the stellar photospheric line C III $\lambda$1176 in the composite where we detect a velocity difference of $-330$ km s$^{-1}$ with respect to Ly$\alpha$. We can thus infer that Ly$\alpha$ emission in our sample is redshifted on average by $\Delta v_{Ly\alpha} = 330$ km s$^{-1}$. In a similar fashion, stacking spectra using the redshift $z_{IS}$ based on low-ionization interstellar absorption results in a detection of C III $\lambda$1176 with a velocity offset of $+190$ km s$^{-1}$. For comparison, at $z \simeq 3$ Steidel et al. (2010) find $\langle \Delta v_{Ly\alpha} \rangle = +445$ km s$^{-1}$ and $\langle \Delta v_{IS} \rangle = -164$ km s$^{-1}$. To construct composite spectra, we use either $z_{Ly\alpha}$ shifted by $-330$ km s$^{-1}$ or $z_{IS}$ shifted by $+190$ km s$^{-1}$ to approximate the systemic redshift of each galaxy. We use the Ly$\alpha$ -based redshift when available since it is typically determined with greater precision than $z_{IS}$. Figure 3 shows the composite spectrum of 81 galaxies in our sample with $3.5 < z < 4.5$ and apparent magnitude $z'_{AB} < 26.0$ using this method.

### 3.1. Uncertainties in the Systemic Redshift

A natural concern is the extent to which these applied shifts might vary within the sample used to make the composite. This can be estimated from observations of higher signal to noise from spectra taken at lower redshift. Steidel et al. (2010) quantify

the offset between $z_{IS}$, $z_{Ly\alpha}$, and the systemic redshift $z_{H\alpha}$ in a sample of 89 galaxies at $z \simeq 2.3$. They find velocity offsets of $\Delta v_{IS} = -170 \pm 115$ km s$^{-1}$ and $\Delta v_{Ly\alpha} = 485 \pm 185$ km s$^{-1}$ relative to H$\alpha$. Assuming this is representative of our data, the uncertainty in our systemic redshift is therefore likely to be $\sigma(v) \sim 150$ km s$^{-1}$. An upper limit on $\sigma(v)$ can be estimated from the width of spectral lines in the composite spectrum. In particular, the rest wavelength of the stellar line C III $\lambda$1176 in the composite provides a valuable measurement of the average offset from the systemic velocity and its width provides an upper limit on the effective spectral resolution. We measure a systemic velocity of $21 \pm 101$ km s$^{-1}$ in the composite spectrum (Figure 3) and an FWHM = 520 km s$^{-1}$ (deconvolved from the instrumental resolution $\simeq$450 km s$^{-1}$). The uncertainty in the adopted redshifts about the true systemic stellar value is therefore $\leqslant$520 km s$^{-1}$ FWHM or equivalently $\sigma(z) \leqslant 220$ km s$^{-1}$, comparable in fact to what was achieved for individual spectra at lower redshift by Steidel et al. (2010).

### 3.2. Error Spectrum

Figure 3 shows the composite spectrum of our sample as well as the $1\sigma$ error spectrum derived using the bootstrap technique discussed above. The error at each pixel is calculated as the standard deviation of all averaged data points (excluding outliers), divided by the square root of the number of data points. There are several wavelength-dependent factors contributing to the error spectrum in addition to the finite signal to noise of individual spectra. One factor is the intrinsic sample variance,
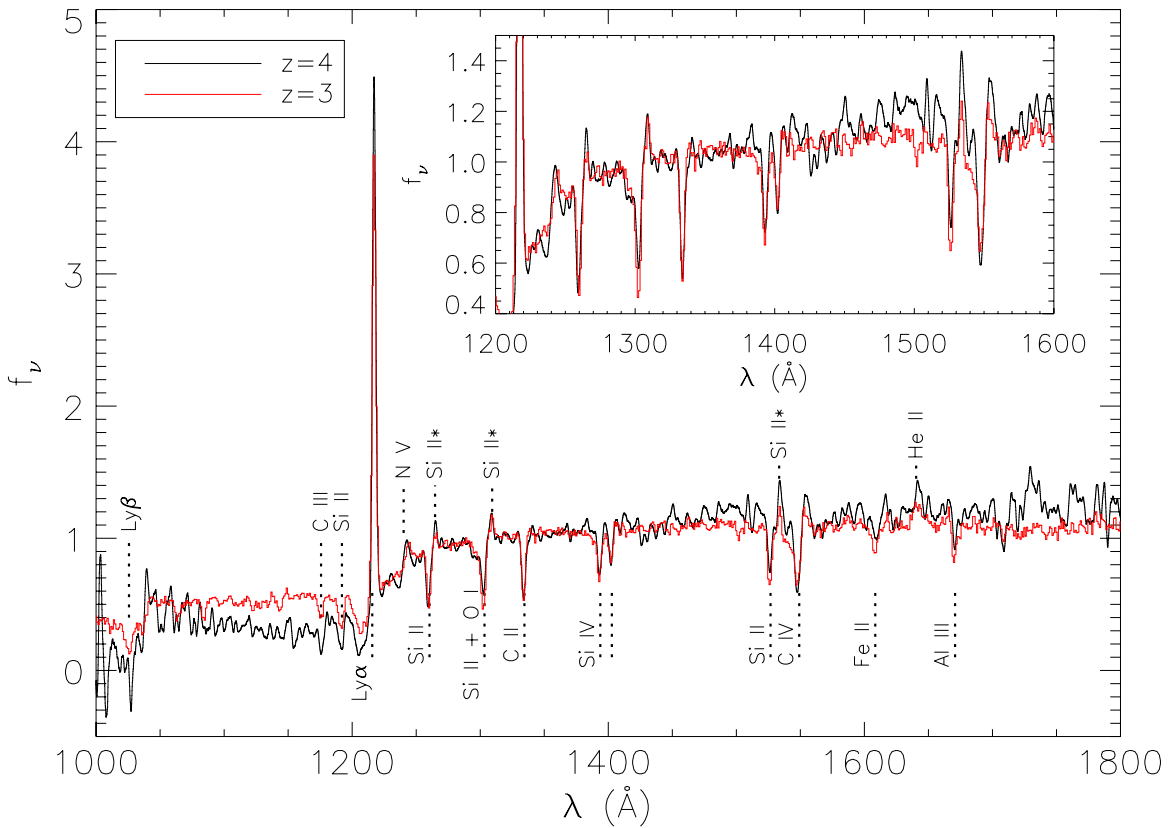
**Figure 4.** Composite spectrum of all 81 galaxies in our sample with $z < 4.5$ and apparent magnitude $z' < 26$, compared to the composite spectrum of 811 LBGs at $z = 3$ presented in Shapley et al. (2003). The higher redshift sample has a much stronger Ly$\alpha$ forest break, slightly redder UV spectral slope, slightly stronger Ly$\alpha$ emission, and weaker absorption lines. The inset shows a zoom-in of the region from 1200 to 1600 Å, which contains most of the absorption lines of interest in this paper.

(A color version of this figure is available in the online journal.)

seen clearly as a noise spike at the position of Ly$\alpha$ and also evident for C II $\lambda$1334 and other absorption features. Another is the decreased instrument throughput at $\lambda \lesssim 6000$ Å, leading to higher noise at shorter wavelengths. Similarly, stronger sky line emission causes increasing noise at longer wavelengths. Finally, the number of contributing spectra peaks at rest frame $\lambda \simeq 1150$–$1350$ Å, with increased noise at higher and lower wavelengths where fewer spectra are included. Our observed wavelength range 5000 Å $< \lambda <$ 9200 Å corresponds to a rest frame 1000 Å $< \lambda <$ 1800 Å at the mean redshift of $z = 3.9$ of our magnitude-limited sample. Ultimately, we achieve a signal-to-noise ratio (S/N) in the continuum of $\geqslant 10$ between the Ly$\alpha$ line and rest frame 1800 Å and $\simeq 5$ in the Ly$\alpha$ forest, with a peak S/N $\simeq 30$ at 1350 Å.

## 4. FEATURES IN THE COMPOSITE SPECTRUM

We now discuss the composite spectrum (Figure 3) in more detail, focusing on the strong spectral features at 1215–1550 Å where we have the best signal to noise. In this wavelength range, we detect Ly$\alpha$, N V $\lambda\lambda$1239,1243, Si II $\lambda$1260, Si II*$\lambda$1265, O I $\lambda$1302+Si II $\lambda$1304 (blended), Si II*$\lambda$1309, C II $\lambda$1334, Si IV $\lambda\lambda$1394,1403, Si II $\lambda$1527, Si II*$\lambda$1533, and C IV $\lambda\lambda$1548, 1550 at high significance. Our $z = 3.9$ composite spectrum is very similar to the composite of $z = 3$ LBGs presented in Shapley et al. (2003), which we show in Figure 4 for comparison. The absolute magnitude distribution of our sample is broadly similar to that at $z = 3$; both cover the range $-22 < M_{\rm UV} < -20$. Our discussion below follows closely that presented originally by

Shapley et al. (2003), but we are also interested in whether there are differences seen over the redshift range $3 < z < 4.5$. We will discuss these possible evolutionary trends in Section 5.

### 4.1. Lyman Break Galaxies: A Physical Picture

It is helpful to begin by describing a possible physical picture of LBGs based on many analyses of the extensive observations at $z \simeq 3$ (see Shapley 2011 for a recent review). Typical $\mathcal{L}^*$ LBGs at $z = 3$ have ultraviolet half-light radii of $\simeq 2.0$ kpc, stellar masses of $\sim 3 \times 10^{10} M_\odot$, and star formation rates of $\sim 50 M_\odot$ yr$^{-1}$ (Bouwens et al. 2004; Ferguson et al. 2004; Shapley et al. 2001). The star formation surface density is sufficient to drive "superwinds" of outflowing gas, similar to those seen in local galaxies where $\Sigma_{\rm SFR} \gtrsim 0.1 M_\odot$ yr$^{-1}$ kpc$^{-2}$ (Heckman 2002). Indeed, blueshifted interstellar absorption lines confirm there are outflows with typical velocities of $\simeq 150$ km s$^{-1}$, and in some cases as high as 800 km s$^{-1}$ (Shapley et al. 2003; Pettini et al. 2002; Quider et al. 2009, 2010). However, the physical origin of these outflows remains unclear (e.g., Murray et al. 2010). It is thought these outflows produce an extended circumgalactic medium (CGM) of ejected material. Outflowing gas is found in both low- and high-ionization states (e.g., Si II and Si IV). Low-ionization transitions such as Si II and C II are mostly associated with neutral hydrogen, whereas high-ionization lines occur in the fully ionized component. Based on trends in the strength of the various species, Shapley et al. (2003) suggest a geometry in which discrete clouds of neutral gas are embedded in a halo of ionized gas. Steidel et al. (2010)
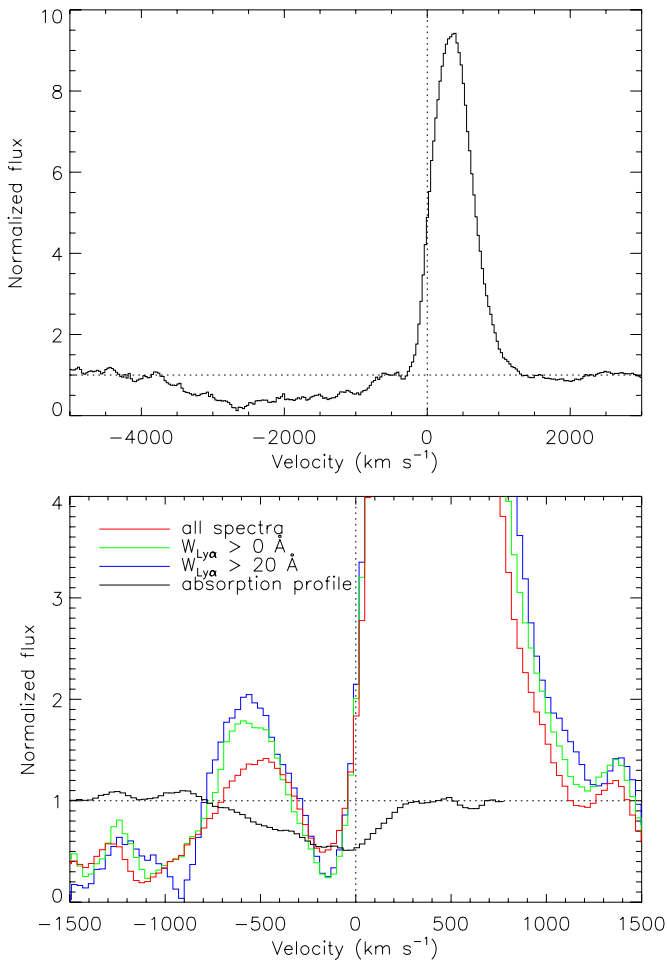
**Figure 5.** Top: composite spectrum normalized to continuum flux levels, showing the velocity structure of Lyα. The line profile consists of a broad blueshifted absorption trough at $v \gtrsim -4000$ km s$^{-1}$ and strong redshifted emission extending to $v = +1000$ km s$^{-1}$. Bottom: velocity profile of Lyα showing a blueshifted secondary peak. The composite spectra in this plot are constructed only from DEIMOS data, with spectral resolution of $R \simeq 2000$. The composites show a blueshifted Lyα emission peak centered at $v = -600$ km s$^{-1}$, corresponding to the maximum outflow velocity of neutral gas as seen in the average velocity profile of low-ionization absorption lines (black). Blueshifted Lyα emission arises from photons scattered at the leading edge of outflowing neutral CGM.

show that the neutral and ionized CGM components both extend to radii of at least 125 kpc.

### 4.2. Lyα

Lyα is the most prominent and diverse feature in our individual spectra. The line originates from hydrogen recombination in H II regions photoionized by massive stars and, as these stars dominate the adjacent continuum, its *intrinsic equivalent width* should be within the range $W_{Ly\alpha} = 100$–$200$ Å for nearly all stellar populations (e.g., Forero-Romero et al. 2012). Our composite spectrum reveals a complex line profile with strong absorption extending blueward to $v = -4000$ km s$^{-1}$, and redshifted emission to $v = +1000$ km s$^{-1}$ (Figure 5) with a peak offset of $v = +330$ km s$^{-1}$ relative to the systemic velocity. The net equivalent width $W_{Ly\alpha} = 21 \pm 3$ Å is only $\lesssim 20\%$ of the expected intrinsic value.

The form of this Lyα profile has been readily understood in terms of the physical picture discussed in Section 4.1. Lyα emission produced at the systemic velocity can escape only

along a line of sight free of neutral hydrogen or if it is shifted in velocity far from resonance. As photons escape, they encounter blueshifted clouds of partially neutral gas, which absorb and re-emit isotropically. Photons backscattered from neutral clouds at small radii will appear *redshifted* and have a higher chance of escaping. Additionally, photons scattered from neutral gas at the edge of the CGM can escape into the ionized intergalactic medium (IGM) and will be observed as blueshifted emission (Steidel et al. 2010). Indeed, Figure 5 shows such a weak blueshifted emission peak in the composite spectrum. On the other hand, the reduced equivalent width compared to that expected intrinsically could be due to many effects including dust extinction, scattering at large radii where emission falls outside the spectroscopic slits, and a non-zero escape fraction $f_{esc}$ of ionizing radiation. Since these effects cannot easily be disentangled, the absolute strength of the Lyα line must be interpreted with caution (Paper II; Schenker et al. 2012).

We can estimate the spatial extent of the neutral CGM (i.e., the radius at which escaping Lyα is last scattered) based on the strength of the diffuse blueshifted Lyα emission. The spatial profile of extended Lyα emission has been well quantified at $z \simeq 2.6$ by Steidel et al. (2011) who find that diffuse halos are a generic property of star-forming galaxies leading to a total Lyα flux $\simeq 5 \times$ greater than that measured within the spectroscopic slits.

Average Lyα surface brightness profiles are well fit at large radii by an exponential form, viz.,

$$\Sigma_{Ly\alpha}(b) = \Sigma_0 \exp(-b/b_l), \qquad (1)$$

where $b_l \simeq 25$ kpc. The blueshifted emission shown in Figure 5 has an equivalent width $W = 1.5 \pm 0.3$ Å measured within a slit aperture of $\simeq 1''.0 \times 1''.0$, corresponding to $7.1 \times 7.1$ kpc$^2$ at $z = 4$. Assuming this approximates the peak value, we estimate that $\Sigma_0 = 1.5 \pm 0.3$ Å per 50 kpc$^2$ and integrating Equation (1) yields a total equivalent width of $W_{halo} = 2\pi b_l^2 \Sigma_0$. Using the measured value of $\Sigma_0$, the scale length is given by

$$b_l = (2.3 \pm 0.2)\sqrt{W_{halo}/\text{Å}}\,\text{kpc}. \qquad (2)$$

Although the total Lyα flux is not measured, we can estimate its value from theoretical expectations as well as observations at lower redshift. The equivalent width in Figure 5 is $W = 21.0$ Å (excluding the blueshifted emission component), thus we can write $W_{halo} = W_{tot} - 21$ Å. As discussed above, the *observed* $W_{tot}$ is diminished by dust and the escape of ionizing radiation. Indeed, Steidel et al. (2011) measure $W_{tot} = 17$–$93$ Å in various subsamples of their data, all lower than the expected intrinsic value, $W_{tot} = 100$–$200$ Å. Considering the composite DEIMOS spectra shown in Figure 5 and assuming an intrinsic $W_{tot} = 135$ Å (Forero-Romero et al. 2012), we derive upper limits of $b_l < 20 \pm 2$ kpc for galaxies with $W_{Ly\alpha} > 0$ and $b_l < 17 \pm 2$ kpc for those with $W_{Ly\alpha} > 20$ Å. This latter constraint is the most stringent and also likely closest to the true value of $b_l$. Steidel et al. (2011) find that their sample of LAEs (defined as $W_{Ly\alpha} > 20$ Å) has the highest $W_{tot}$ (=93 Å) and largest scale length ($b_l = 28.4$ kpc) of any subsample that they analyze. Our constraint of $b_l < 17$ kpc for the LAEs therefore suggests that the characteristic size of Lyα halos may be smaller at $z = 4$ than at $z = 2$–$3$.

While the analysis above suggests that Lyα halos surrounding star-forming galaxies may be smaller at higher redshifts, direct measurements of low surface brightness Lyα emission are

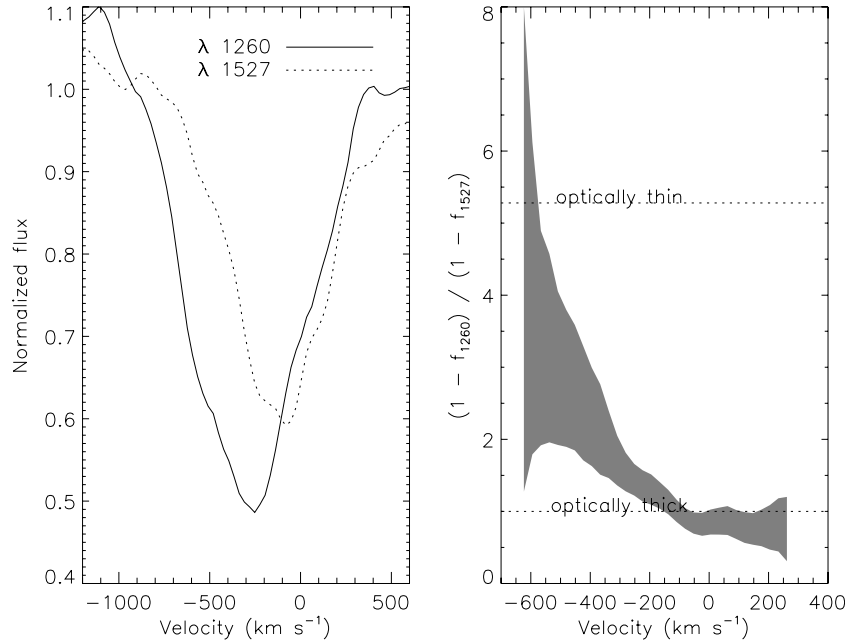**Figure 6.** Left: comparison of the absorption line profiles for Si II transitions at 1260 and 1527 Å in our composite spectrum. Right: the profile ratio $(1 - f_{1260})/(1 - f_{1527})$ with the optically thick and thin regimes indicated; the shading refers to the $1\sigma$ uncertainty. Although both transitions are optically thick at low velocities $|v| < 200$ km s$^{-1}$, there is some evidence of optically thin gas at $|v| > 200$ km s$^{-1}$.

needed to confirm this possibility. We therefore attempt to measure the characteristic scale length of Ly$\alpha$ halos in our sample from two-dimensional spectra. To do so, we construct a composite DEIMOS spectrum using the sample of objects as in Figure 5 (bottom panel). Each two-dimensional spectrum is normalized by the same $f_\nu$ value and interpolated to the same common rest-frame wavelength scale as described in Section 3. Additionally, the continuum centroid position is used to spatially align each spectrum. The composite is then created by averaging spectra at each point in position and wavelength using the $\sigma$-clipped mean method described in Section 3. In the resulting composite, the ultraviolet continuum is detected at impact parameters $b \lesssim 10$ kpc. To avoid uncertain contamination from the continuum, we fit an exponential profile (Equation (1)) to the extended Ly$\alpha$ emission at impact parameters $b \gtrsim 10$ kpc. From the best fit, we obtain a constraint on the scale length of $b_l = 15^{+45}_{-15}$ kpc. While consistent with the values from Steidel et al. (2011), our data clearly lack the precision to directly measure whether the characteristic $b_l$ changes significantly from $z = 2.6$ to $z = 4$. The low sensitivity arises in part from a lack of data at large impact parameters due to small slit lengths. The median usable slit length of $5''.4$ corresponds to impact parameters of only $b \lesssim 20$ kpc, comparable to $b_l$. Sensitive data at larger impact parameters are needed to directly determine the spatial extent of Ly$\alpha$ emission at these high redshifts.

### 4.3. Low-ionization Metal Transitions

According to the physical picture in Section 4.1, absorption in low-ionization transitions occurs in both the interstellar medium and outflowing clouds of cool gas. The former is at the systemic velocity while the latter is blueshifted. Such transitions are generally saturated (Shapley et al. 2003; Pettini et al. 2002), so the line depth at a given velocity provides a measure of the areal covering fraction $f_c$ of O and B stars by neutral gas along the line of sight. Specifically, the line profile is given by $f(v) = f_0 \cdot (1 - f_c(v))$, where $f_0$ is the continuum flux.

While typical LBGs are too faint for detailed line profiles, high-resolution spectra of a few bright lensed sources at $z = 2$–3 (Pettini et al. 2002; Quider et al. 2009, 2010) have revealed absorption velocities ranging from $\sim{-}1000$ to $+500$ km s$^{-1}$ with the highest covering fraction at $v \sim -200$ km s$^{-1}$. The mean low-ionization absorption line velocity offset in our composite is $v_{\rm LIS} = -190$ km s$^{-1}$, in good agreement with that at $z = 2$–3 (Shapley et al. 2003; Steidel et al. 2010).

Of particular diagnostic value are the two relatively unblended transitions of Si II at 1260 and 1527 Å whose equivalent width ratio is a valuable tracer of the optical depth (Shapley et al. 2003). The profiles of both lines and their ratio are shown in Figure 6. Gas near the systemic velocity ($|v| < 200$ km s$^{-1}$) is clearly optically thick, while for $v < -200$ km s$^{-1}$ it is intermediate in optical depth. This difference is also seen in high-resolution spectra of lensed galaxies (Pettini et al. 2002; Quider et al. 2010), and optically thin gas is seen at large galactocentric radii (Steidel et al. 2010) suggesting that smaller, optically thin clouds are more easily accelerated to high velocity and large distances. We note that the column density at which both Si II transitions become optically thick ($\tau > 1$) is $N_{\rm Si\,II} = 1.9 \times 10^{12}$ cm$^{-2}$. Assuming $\log({\rm Si\,II/H}) = -4.86$ as measured for the lensed galaxy cB58 (Pettini et al. 2002), we estimate that optically thin absorption occurs in clouds with hydrogen column densities of $N_{\rm H\,I} \lesssim 10^{17}$ cm$^{-2}$.

#### 4.3.1. Fine Structure Transitions

A satisfying aspect of our composite spectrum is the successful identification of fine-structure emission lines of Si II (see marked features in Figure 3). Si II ions in the CGM absorb photons in the resonance transitions and immediately re-emit a photon at approximately the same velocity. A photon absorbed at 1260 Å will be re-emitted at either the same wavelength or to the fine-structure transition Si II* $\lambda 1265$. Likewise, a photon absorbed at 1527 Å will be re-emitted as either Si II $\lambda 1527$ or Si II* $\lambda 1533$, and an absorbed Si II $\lambda 1304$ photon can be re-emitted as Si II* $\lambda 1309$. In all three cases, the probability of

emission in the resonant and fine-structure transitions is approximately equal.

Since no absorption is seen in the fine-structure transitions, we infer that atoms in the excited ground state will typically decay to the ground state before absorbing another photon. Since every absorbed photon is re-emitted, the net equivalent width of the resonant and fine-structure transitions is $W_{\mathrm{Si\,II}} + W_{\mathrm{Si\,II*}} = 0$. The precise equivalent widths depend on the initial absorption $W_{\mathrm{Si\,II,abs}}$ and the optical depth. If the gas is optically thin, then re-emitted photons will immediately escape giving $W_{\mathrm{Si\,II,em}} = W_{\mathrm{Si\,II*,em}} = -0.5 W_{\mathrm{Si\,II,abs}}$. In the limit of optically thick gas, resonant photons will be continuously scattered until they emerge as Si II* (after two scatterings on average). In this case, $W_{\mathrm{Si\,II,em}} = 0$ and $W_{\mathrm{Si\,II*,em}} = -W_{\mathrm{Si\,II,abs}}$. Since the majority of absorption occurs in optically thick gas (Section 4.3), we expect the equivalent width of Si II absorption lines to reflect the kinematics and covering fraction of neutral gas with minimal contamination from Si II re-emission.

### 4.3.2. The Spatial Extent of Low-ionization Absorption

From the picture above (Section 4.3.1), we expect that the equivalent width of the fine-structure emission lines should be equal and opposite to the resonant line equivalent width. This is not the case: $W_{1265}/W_{1260} = -0.56 \pm 0.36$ and $W_{1533}/W_{1527} = -0.52 \pm 0.20$. ($W_{1309}/W_{1304}$ is more difficult to quantify since Si II $\lambda 1304$ is blended with O I $\lambda 1302$.) There are two possible explanations. One is that scattered photons have larger path lengths and are subject to greater dust attenuation. Since the UV continuum slopes imply little differential extinction (mean $E(B - V) = 0.10$) and we expect only two scatterings for the average Si II* photon, this seems unlikely. More reasonably, the emitting region could be larger than that sampled by our slits. Although the $1''.0 \times 1''.0$ slit aperture samples most of the continuum light and its line of sight absorption, the CGM which absorbs and isotropically re-emits scattered photons extends to much larger radii (Steidel et al. 2010, 2011). The strength of fine-structure emission provides a direct measurement of the amount of absorption at small radii contained within the slit. The fine structure to resonant absorption line ratio suggests that a fraction $0.53 \pm 0.17$ (combining both $\lambda 1265$ and $\lambda 1527$ measures) of the total fine-structure emission is contained within the extraction aperture of 1 arcsec$^2$. The half-light radius of Si II* emission, and hence Si II absorption, thus corresponds to $\sim 0''.5 = 3.5$ kpc at $z = 4$. This scale is only slightly larger than the median half-light radius $r_h = 0''.31$ of galaxies in our sample and would be reached in only 20 Myr at the typical outflow velocity (190 km s$^{-1}$).

It is instructive to reconsider the $z = 3$ composite spectrum from Shapley et al. (2003) where the fine-structure lines are clearly seen (but were not interpreted fully along the discussion above at the time). The Si II* lines are noticeably stronger in our $z \simeq 4$ composite, with an average $W_{\mathrm{Si\,II*}} = 0.7 \pm 0.2$ at $z \simeq 4$ compared to $0.30 \pm 0.05$ Å at $z = 3$. Furthermore, the Si II absorption lines are *weaker* in the $z = 4$ composite, suggesting that the absorption takes place at larger radii at $z = 3$. This difference cannot be explained through instrumental differences between the two surveys. Smoothing our $z = 4$ composite to match the 3.25 Å resolution of Shapley et al. (2003) reduces the equivalent widths by $<5\%$. Likewise, the wider slits used for the $z = 3$ data ($1''.4$, 11 kpc) compared to the $z = 4$ data ($1''.0$; 7 kpc) is not the cause. If the CGM properties are similar, then we expect the fine-structure strength to constitute a *larger* fraction of the resonant absorption line strength in the $z = 3$ data, contrary to

observations. Defining $R_{\mathrm{FS}} = -(W_{1265} + W_{1533})/(W_{1260} + W_{1527})$, we find $R_{\mathrm{FS}} = 0.53 \pm 0.17$ for the $z = 4$ composite spectrum and $R_{\mathrm{FS}} = 0.16 \pm 0.04$ for $z = 3$, indicating a smaller characteristic radius of fine-structure emission at $z = 4$.

Inescapably, therefore, we conclude that the circumgalactic gas around LBGs at $z = 4$ differs in two important ways from that at $z = 3$: there is *greater low-ionization absorption* at small radii at $z = 4$ and *less total low-ionization absorption*. In addressing the origin of this effect, Figure 10 shows that the difference in equivalent width is at least partially linked to the kinematic offset from the Ly$\alpha$ emission. Thus, it seems that a higher covering fraction at small radii is required to produce the stronger fine-structure emission. Higher resolution observations of individual bright, or perhaps gravitationally lensed, galaxies at $z \simeq 4$ will ultimately be required to separate the relative contributions of covering fraction and kinematics in explaining this result.

### 4.4. High-ionization Lines

The high-ionization lines Si IV and C IV arise both in interstellar gas and in stellar P-Cygni winds. The velocity centroid of Si IV, $v = 140$ km s$^{-1}$, is consistent with the low-ionization interstellar absorption lines, suggesting that most absorption is interstellar in origin. This is supported by the absence of a significant redshifted emission component expected for a P-Cygni profile. In contrast, C IV is broader, with a larger absorption velocity offset $v = -370$ km s$^{-1}$ and redshifted P-Cygni emission indicating a large contribution from stellar winds. We also detect the N V $\lambda\lambda 1239, 1243$ P-Cygni feature, although the proximity to Ly$\alpha$ makes this feature difficult to study in detail.

We can determine the optical depth of highly ionized outflowing gas from the ratio of Si IV absorption lines. The ratio $W_{\mathrm{Si\,IV}\lambda 1394}/W_{\mathrm{Si\,IV}\lambda 1403} = 2.0$ for optically thin absorption, and 1.0 in the optically thick case. Shapley et al. (2003) find optically thin absorption in composite spectra of LBGs at $z = 3$, whereas we measure a ratio of $1.4 \pm 0.4$ in the composite spectrum shown in Figure 3 indicating a significant contribution of optically thick absorption at $z \sim 4$. The total equivalent width of the Si IV doublet is weaker by a factor of $0.72 \pm 0.12$ in Figure 3 compared to the $z = 3$ composite of Shapley et al. (2003). The combination of higher optical depth and lower equivalent width suggests that the velocity range and/or covering fraction of the ionized gas traced by Si IV is lower at higher redshift.

### 4.4.1. Metallicity

The P-Cygni profile of C IV is sensitive to metallicity, and the combination of C IV and He II equivalent widths constrains both the age and metallicity. Here, we compare the equivalent widths measured in the composite spectrum (Figure 3) with theoretical models in order to estimate the typical metallicity of galaxies in our sample. We note that the equivalent width of C IV contains significant interstellar absorption, so the value reported in Table 1 should be treated as an upper limit on the P-Cygni component. Assuming that the interstellar absorption component of C IV is similar to that of Si IV ($W \simeq 1.0$ Å), we take the P-Cygni absorption component to have an equivalent width $-1.6 \pm 1.0$ Å with a conservative uncertainty. We compare this estimate and the measured equivalent width of He II (reported in Table 1) with predictions from the stellar population synthesis code BPASS presented in Eldridge & Stanway (2009). We consider BPASS models which include binary evolution with continuous star formation rate and determine the difference $\Delta W$ between observed and predicted equivalent width as a function
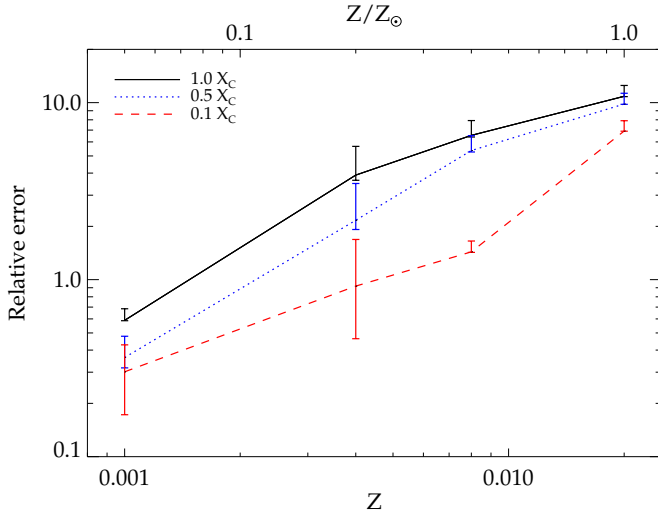
**Figure 7.** Relative error in the equivalent widths of C IV and He II predicted by the stellar population synthesis code BPASS and values measured for the composite spectrum shown in Figure 3 (see the text for details). Relative error values $\lesssim 1$ indicate good agreement. Model results for a range of metallicity $Z$ and carbon depletion factor $X_C$ as a function of age are described in Eldridge & Stanway (2011). The values $X_C = 0.5\ (0.1)$ correspond to a carbon abundance reduced by a factor of 2 (10) relative to solar abundance ratios. Lines are plotted for the median age of our sample ($10^{8.5\pm0.6}$ years) determined from spectral energy density models with the same initial mass function and star formation history used in BPASS, and error bars indicate the allowed range for ages within $1\sigma$ of the median. Measurements of C/O abundance at both low and high redshifts indicate carbon depletion factors $X_C \simeq 0.2$–$0.5$ in galaxies with $Z < 0.2\,Z_\odot$ (e.g., Erb et al. 2010). For this range of $X_C$, models with $Z \lesssim 0.004$ (equivalent to $Z = 0.2\,Z_\odot$) are in good agreement with the data. Solar metallicity models are unable to reproduce the observed equivalent widths.

(A color version of this figure is available in the online journal.)

**Table 1**
Equivalent Width and Velocity of Absorption and Emission Lines in the
Composite Spectrum (Figure 3)

| Ion | $\lambda_{\rm rest}$ (Å) | $W$ (Å) | $v_{\rm cen}$ (km s$^{-1}$) |
|---|---|---|---|
| C III | 1175.71 | $-2.4 \pm 0.8$ | $21 \pm 101$ |
| H I | 1215.67 | $20.9 \pm 2.9$ | $376 \pm 13$ |
| Si II | 1260.42 | $-1.4 \pm 0.3$ | $-281 \pm 38$ |
| Si II* | 1264.74 | $0.9 \pm 0.3$ | $89 \pm 61$ |
| O I + Si II | 1303.27 | $-1.6 \pm 0.3$ | $-258 \pm 62$ |
| Si II* | 1309.28 | $0.7 \pm 0.2$ | $-118 \pm 80$ |
| C II | 1334.53 | $-1.6 \pm 0.2$ | $-136 \pm 39$ |
| Si IV | 1393.76 | $-1.1 \pm 0.2$ | $-122 \pm 50$ |
| Si IV | 1402.77 | $-0.8 \pm 0.2$ | $-160 \pm 45$ |
| Si II | 1526.71 | $-1.3 \pm 0.3$ | $-99 \pm 54$ |
| Si II* | 1533.43 | $0.8 \pm 0.3$ | $114 \pm 64$ |
| C IV | 1549.48 | $-2.6 \pm 0.4$ | $-374 \pm 57$ |
| He II | 1640.40 | $1.3 \pm 0.7$ | $141 \pm 282$ |

of metallicity and relative carbon abundance. We restrict the stellar population age to be within the $1\sigma$ scatter of the median value for galaxies in our sample, determined to be $10^{8.5\pm0.6}$ years from spectral energy density fits assuming constant star formation with a Kroupa (2002) initial mass function. Figure 7 shows the resulting relative error between BPASS models and the measured equivalent width, which we define as

$$\text{Relative error} = 0.5\left[\left(\frac{\Delta W_{\rm C\,IV}}{\sigma_{\rm C\,IV}}\right)^2 + \left(\frac{\Delta W_{\rm He\,II}}{\sigma_{\rm He\,II}}\right)^2\right]. \quad (3)$$

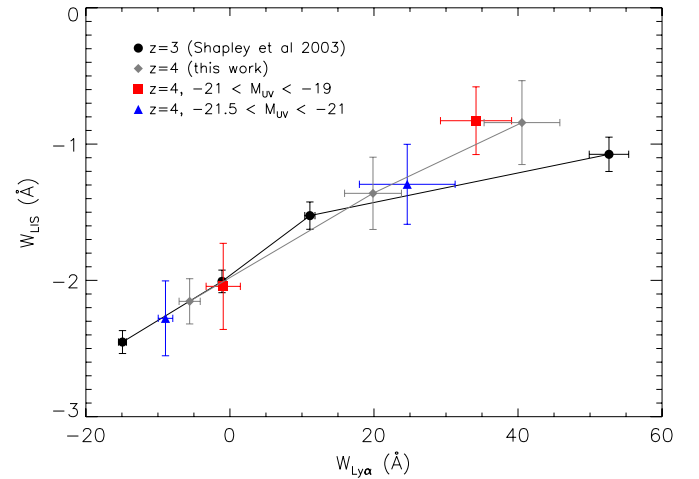Relative error values $\lesssim 1$ are thus consistent with the data.



**Figure 8.** Equivalent width of low-ionization absorption lines compared to that of Ly$\alpha$. Gray diamonds are from our sample at $z \simeq 4$ divided into bins of $W_{\rm Ly\alpha} < 0$, $W_{\rm Ly\alpha} = 0$–$40$ Å, and $W_{\rm Ly\alpha} > 40$ Å. Black circles show the sample of Shapley et al. (2003) at mean $z = 3$, divided into quartiles of $W_{\rm Ly\alpha}$. Galaxies in the $z = 3$ sample have typical luminosities $-21.5 < M_{\rm UV} < -21.0$ corresponding to the blue triangles. Galaxies of the same luminosity lie on the same correlation between $W_{\rm Ly\alpha}$ and $W_{\rm LIS}$ at both $z = 3.9$ and $z = 3$. Fainter galaxies have weaker low-ionization absorption lines at fixed $W_{\rm Ly\alpha}$.

(A color version of this figure is available in the online journal.)

Models with $Z \leqslant 0.004$ and somewhat depleted carbon abundance are in good agreement with the data. We note that observations of both local and high-redshift galaxies indicate typical relative carbon abundances (C/O) $\simeq 2$–$5\times$ lower than the solar value (equivalent to $X_C = 0.2$–$0.5$ in Figure 7) for metallicities of $Z \lesssim 0.004$ (Kobulnicky & Skillman 1998; Shapley et al. 2003; Erb et al. 2010; Eldridge & Stanway 2011). Solar metallicity models ($Z = 0.020$) do not fit the data. We conclude that the typical metallicity of galaxies in our sample is $Z \lesssim 0.004$ or $\lesssim 0.2\times$ solar metallicity. Bright galaxies at $z < 3.8$ in the FORS2 sample have gas-phase metallicity of $12 + \log({\rm O/H}) = 7.7$–$8.5$ or about $0.1$–$0.6\times$ the solar value, in reasonable agreement (Maiolino et al. 2008). These values are consistent with the allowed metallicity range $0.1 < Z/Z_\odot < 0.6$ inferred for the Shapley et al. (2003) composite using the same BPASS models (Eldridge & Stanway 2011). Given that the equivalent widths of C IV and He II in Shapley et al. (2003) agree well with those in Table 1, we expect the typical metallicity of galaxies to be similar in both samples.

## 5. SPECTROSCOPIC TRENDS

We now turn to an analysis of how the various spectroscopic features discussed in Section 4 are related to observable properties of LBGs as a prelude to considering how they might evolve with redshift. We will begin with the dependence of low-ionization absorption line strength with Ly$\alpha$ equivalent width. This is motivated by the common physical dependence of these features—both are governed by the kinematics and covering fraction of neutral circumgalactic gas—and also because this has been examined in detail for LBGs at $z = 3$ (Shapley et al. 2003).

We construct composite spectra of three subsamples of galaxies divided according to their Ly$\alpha$ equivalent width. Defining $W_{\rm LIS}$ as the average equivalent width of $\lambda 1260$, $\lambda 1303$, $\lambda 1334$, and $\lambda 1527$ Å features, Figure 8 shows weaker $W_{\rm LIS}$ for galaxies with stronger Ly$\alpha$. This was also noted for $z = 4$ LBGs by Vanzella et al. (2009). Both the $z = 3$ and $z = 4$ samples
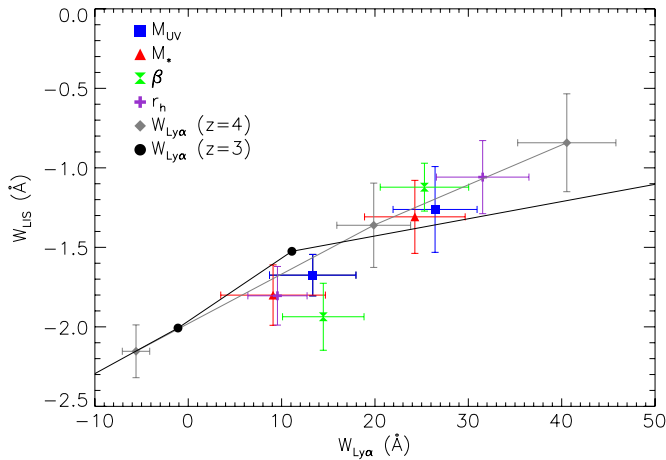
**Figure 9.** Equivalent width of low-ionization absorption lines compared to that of Ly$\alpha$, divided according to observable demographic properties as described in the text. Points binned by $W_{Ly\alpha}$ at $z = 3$ and $z = 4$ are the same as in Figure 8. The sample was divided into two bins for each demographic property ($M_{UV}$, $M_*$, $\beta$, and $r_h$), with $W_{Ly\alpha}$ and $W_{LIS}$ measured from composite spectra of the galaxies in each bin.

(A color version of this figure is available in the online journal.)

show this trend, although $W_{LIS}$ is weaker at $z = 4$ for galaxies with strong Ly$\alpha$ emission. This difference can be attributed to the luminosity-dependent trend of stronger $W_{Ly\alpha}$ and weaker $W_{LIS}$ in fainter galaxies (Paper I; Shapley et al. 2003; Vanzella et al. 2009). If we consider a subset of galaxies in our sample with similar absolute magnitudes to those observed at $z = 3$ ($-21.5 < M_{UV} < -21.0$), then we recover the same normalization (Figure 8). Our sample is 90% complete at the corresponding apparent magnitudes, so we expect a negligible bias.

Having established the correlation of $W_{LIS}$ with $W_{Ly\alpha}$, we now examine the dependence with other demographic properties. We divide the full sample into two bins of equal size according to each property of interest. The results are shown in Figure 9. We briefly review the trend of each property with $W_{LIS}$ and $W_{Ly\alpha}$ and discuss the physical origin. Many of these trends were seen in Shapley et al. (2003) and Vanzella et al. (2009) and are clearly inter-related due to correlations between the demographic properties.

Less luminous galaxies have stronger $W_{Ly\alpha}$ and weaker $W_{LIS}$, illustrating that higher star formation rates drive larger amounts of neutral gas into the CGM with higher velocity and/or covering fraction. Defining the ultraviolet spectral slope as $\beta = 5.30 \cdot (i_{AB} - z_{AB}) - 2.04$ for $B$-drops (Bouwens et al. 2009), we also find that bluer galaxies with lower $\beta$ have stronger $W_{Ly\alpha}$ and weaker $W_{LIS}$. This trend was also noted in Paper I, which showed that LBGs with strong Ly$\alpha$ emission have systematically bluer $\beta$. Since neutral gas also presumably contains dust, the same gas which gives rise to $W_{LIS}$ also reddens the continuum. Stellar masses $M_*$ are measured for 60% of our sample for which there is unconfused *Spitzer*/IRAC photometry. As expected from the trends with luminosity, lower mass galaxies have stronger $W_{Ly\alpha}$ and weaker $W_{LIS}$. Finally, measuring half-light radii $r_h$ from the GOODS ACS data with SEXTRACTOR, we find smaller galaxies have stronger $W_{Ly\alpha}$ and weaker $W_{LIS}$.

Could these trends be due to selection effects or sample bias? The trend of stronger Ly$\alpha$ for less luminous LBGs is of particular concern, since fainter galaxies will require a larger $W_{Ly\alpha}$ for detection. To address this, we consider only the 32 galaxies with apparent magnitudes of $z'_{AB} < 25$ for which the spectroscopic

sample is 90% complete. This subsample is divided into two equal bins and the results confirm that trends seen in the larger sample also hold in brighter galaxies unaffected by sample bias.

The trends shown in Figure 9 are generally consistent with the overall trend of $W_{LIS}$ with $W_{Ly\alpha}$ (Figure 8). The $W_{Ly\alpha}$ variations mostly arise from the distribution of neutral gas (traced by $W_{LIS}$), with relatively little effect from other demographic properties examined ($M_{UV}$, $\beta$, $M_*$, $r_h$). However, demographic properties do have some effect. The strongest deviation seen in Figure 9 is that with $\beta$, which shows stronger $W_{LIS}$ than would be expected at a given $W_{Ly\alpha}$ for galaxies with red UV slopes. Noted also by Shapley et al. (2003), this suggests that outflowing neutral gas contains dust which reddens the continuum. Also, more luminous galaxies (i.e., those with higher star formation rates) have stronger $W_{LIS}$ at a given $W_{Ly\alpha}$ (Figure 8). This is likely due to increased absorption at large velocities in galaxies with higher star formation rate, as observed at $z \simeq 1.4$ (Weiner et al. 2009). For all other demographics, the composite spectra have values of $W_{LIS}$ within $1\sigma$ of that expected purely based on $W_{Ly\alpha}$.

In summary, the trends seen in Figure 9 arise almost entirely because of variations in the neutral gas covering fraction and/or kinematics, which are themselves correlated with the demographic properties.

### 5.1. Kinematics

We have now established that outflowing neutral gas is the dominant factor in determining both $W_{Ly\alpha}$ and $W_{LIS}$. However, variations from the trend of $W_{LIS}$ with $W_{Ly\alpha}$ are apparent, particularly with $\beta$ and $M_{UV}$ as discussed above. The most obvious mechanism for this behavior is a systematic difference in the covering fraction $f_c$ and kinematics of neutral gas. Assuming $W_{LIS} \propto \int f_c(v)dv$ (where $v$ is the outflow velocity), a higher $f_c$ and lower velocity range can conspire to give a constant $W_{LIS}$. However, changing $f_c$ and $v$ will also affect the transmission of Ly$\alpha$ photons resulting in a different $W_{Ly\alpha}$. It is therefore of interest to consider how to distinguish between the covering fraction and kinematics of neutral gas.

The kinematics of neutral gas can be roughly parameterized by the velocity dispersion and centroid of low-ionization interstellar absorption lines. We have measured the velocity $\Delta v$ of low-ionization absorption lines with respect to Ly$\alpha$ as a proxy for outflow velocity. $\Delta v$ is strongly correlated with $W_{Ly\alpha}$ and $W_{LIS}$ in LBGs at $z = 3$ (Shapley et al. 2003) in the sense that larger velocities are associated with stronger interstellar absorption and weaker Ly$\alpha$ emission. Figure 10 shows $\Delta v$ measured from the same composite spectra used to determine demographic trends (e.g., Figure 9), as well as the results from Shapley et al. (2003). All $z \simeq 4$ composites are consistent (within $1\sigma$) with the relation measured at $z = 3$, as well as the mean $\Delta v$ measured for $B$-dropout galaxies by Vanzella et al. (2009). We measure a velocity dispersion for each composite and find that each is within $1.2\sigma$ of the effective spectral resolution $\sigma = 290$ km s$^{-1}$ (measured for the stellar [C III] feature in Figure 3). We are therefore unable to detect trends in outflow kinematics with demographic properties in composite spectra. Higher signal-to-noise data, higher spectral resolution, or detailed studies of individual galaxies are required to address trends in kinematics and the covering fraction of neutral gas at $z = 4$.

### 6. THE EVOLVING CGM

We now turn to a discussion of the redshift evolution of the neutral CGM surrounding typical LBGs. The most useful
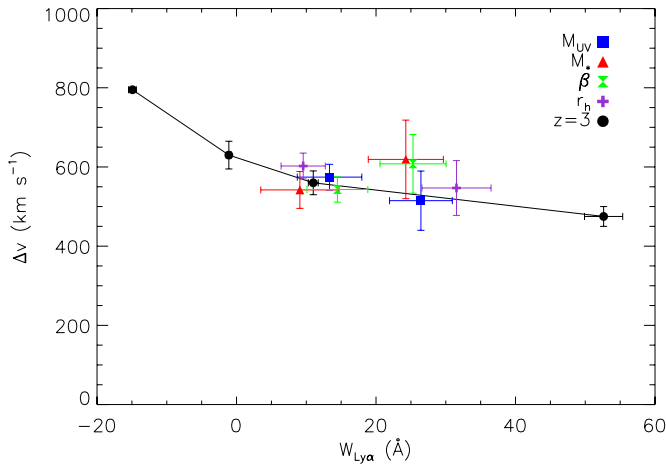
**Figure 10.** Kinematic offset $\Delta v$ between Ly$\alpha$ emission and low-ionization absorption lines, as a function of $W_{\text{Ly}\alpha}$. The composites used to measure $\Delta v$ and $W_{\text{Ly}\alpha}$ are the same as in Figure 9. Data at $z = 3$ are from Shapley et al. (2003). (A color version of this figure is available in the online journal.)
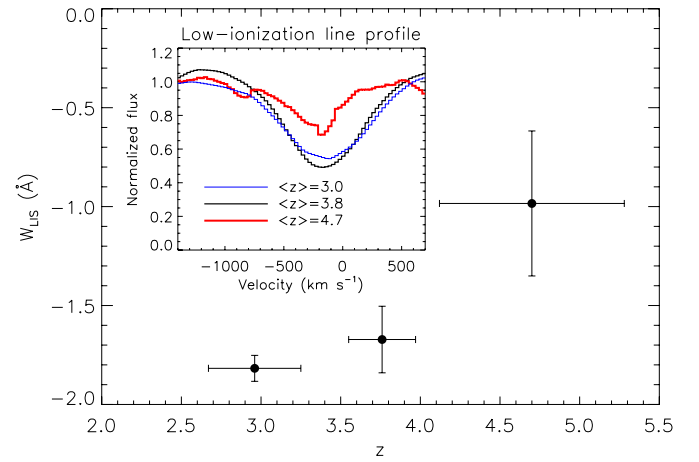


**Figure 11.** Equivalent width of low-ionization absorption lines measured from composite spectra of LBGs at different redshifts. The DEIMOS and FORS2 data presented in this paper are separated into two subsamples of equal size as described in the text. We also show the equivalent result at $z = 3$ from the composite spectrum of Shapley et al. (2003), with redshift distribution described in Steidel et al. (2003). The average low-ionization line profile of each composite is shown in the inset. Low-ionization absorption lines are significantly weaker for galaxies in the highest redshift composite. All three samples have consistent mean luminosity and $W_{\text{Ly}\alpha}$.

(A color version of this figure is available in the online journal.)

**Table 2**
Mean Demographic and Spectroscopic Properties of LBGs at Different Redshifts

| Property | $z < 4.1$ | $z > 4.1$ |
|---|---|---|
| $z$ | $3.76 \pm 0.21$ | $4.70 \pm 0.58$ |
| $M_{\text{UV}}$ | $-21.0 \pm 0.3$ | $-21.0 \pm 0.3$ |
| $\log M_*/M_\odot$ | $9.6 \pm 0.6$ | $9.8 \pm 0.6$ |
| $r_h$ (kpc) | $2.42 \pm 0.97$ | $1.94 \pm 0.74$ |
| $\beta$ | $-2.02 \pm 0.08$ | $-2.12 \pm 0.19$ |
| $W_{\text{Ly}\alpha}$ (Å) | $15.4 \pm 5.9$ | $12.2 \pm 3.7$ |
| $W_{1260}$ (Å) | $-1.7 \pm 0.4$ | $-0.7 \pm 0.4$ |
| $W_{1265}$ (Å) | $0.8 \pm 0.3$ | $1.0 \pm 1.0$ |
| $W_{1303}$ (Å) | $-2.1 \pm 0.4$ | $-0.9 \pm 0.4$ |
| $W_{1309}$ (Å) | $1.0 \pm 0.3$ | $0.9 \pm 0.4$ |
| $W_{1334}$ (Å) | $-1.7 \pm 0.3$ | $-1.7 \pm 0.9$ |
| $W_{1527}$ (Å) | $-1.2 \pm 0.3$ | $-0.6 \pm 1.0$ |
| $W_{1533}$ (Å) | $0.7 \pm 0.3$ | $0.9 \pm 0.5$ |

**Notes.** Error bars correspond to the standard deviation of values for individual galaxies in each subsample. $\beta$ and equivalent widths of Ly$\alpha$ and low-ionization metal transitions are measured directly from composite spectra, with error bars determined from a bootstrap method (see the text for details).

probes are Ly$\alpha$ and low-ionization absorption lines which trace the kinematics and covering fraction of neutral gas, and fine-structure emission lines which provide a constraint on the spatial extent of the absorbing gas (Section 4.3.2).

The common dependence of Ly$\alpha$ and low-ionization absorption lines on the neutral CGM results in a strong correlation between $W_{\text{LIS}}$ and $W_{\text{Ly}\alpha}$. Various physical properties of LBGs are correlated with both $W_{\text{LIS}}$ and $W_{\text{Ly}\alpha}$, but in such a way that the relation between $W_{\text{LIS}}$ and $W_{\text{Ly}\alpha}$ remains nearly constant (Figure 9). Furthermore, the $W_{\text{LIS}}$–$W_{\text{Ly}\alpha}$ relation at fixed $M_{\text{UV}}$ does not change significantly with redshift between $z = 3$ and $z = 4$ (Figure 8).

To further examine evolutionary trends with redshift, we now divide our spectroscopic sample into two bins of redshift at fixed $M_{\text{UV}}$, now including galaxies at all redshifts (no longer restricted to $z < 4.5$ as in previous sections). We consider galaxies with absolute magnitude $-21.5 < M_{\text{UV}} < -20.5$, chosen to be representative of the sample in Shapley et al. (2003). There are 64 galaxies in our sample within this $M_{\text{UV}}$ range (see Figure 2). We construct composite spectra of galaxies with redshift above and below the median $z = 4.1$ and measure the equivalent width of Ly$\alpha$ and low-ionization lines (both resonant absorption and fine-structure emission) in each composite. The results are given in Table 2, along with the demographic properties of galaxies in each subsample. The quantities $M_{\text{UV}}$, $M_*$, and $r_h$ are measured from photometry while $\beta$ is determined from a direct fit to the ultraviolet continuum in the composite spectrum. We define $f_\lambda \propto \lambda^\beta$ and fit the rest frame 1300–1700 Å to determine $\beta$, with uncertainty quantified using the bootstrap method described in Section 3. Aside from redshift, the demographics of each subsample are quite similar. The higher redshift galaxies have slightly higher average $M_*$, smaller $r_h$, and smaller (bluer) $\beta$. $W_{\text{Ly}\alpha}$ is consistent for both to within the sample variance and is also consistent with the value $W_{\text{Ly}\alpha} = 14.3$ Å measured for the composite spectrum of $z = 3$ LBGs in Shapley et al. (2003). The most striking difference is in the strength of the low-ionization absorption lines, which are significantly weaker at higher redshifts (Figure 11). The variation in $W_{\text{LIS}}$ is *not* explained by systematic differences in $W_{\text{Ly}\alpha}$ or demographic properties, and hence we seek an alternate explanation.

We first examine whether the evolution in $W_{\text{LIS}}$ could arise as a result of different equivalent width distributions for Ly$\alpha$.

Although the mean $W_{\text{Ly}\alpha}$ across our two redshift subsamples is similar, the lower redshift subsample has a broader distribution and contains more galaxies with Ly$\alpha$ in absorption ($W_{\text{Ly}\alpha} < 0$). This is reflected in the larger sample variance in $W_{\text{Ly}\alpha}$ at lower redshift (Table 2). We evaluate the effect of this potential bias on $W_{\text{LIS}}$ by constructing a composite spectrum from a subset of the $z < 4.1$ galaxies with intermediate $W_{\text{Ly}\alpha} = 0$–30 Å, resulting in a consistent mean $W_{\text{Ly}\alpha}$ with sample variance reduced by a factor of 2.5. This composite has $W_{\text{LIS}} = -1.5$ Å, 0.2 Å higher than when the full range of $W_{\text{Ly}\alpha}$ is used, but still considerably lower than the value $W_{\text{LIS}} = -1.0$ Å measured for the higher redshift galaxies. We therefore conclude that differences in the $W_{\text{Ly}\alpha}$ distribution are insufficient to explain the observed variation in absorption line strength with redshift.

There are several possible physical explanations for the evolution of $W_{\text{LIS}}$ with redshift shown in Figure 11. One possibility

is that the kinematics and/or covering fraction of neutral gas are systematically different. For example, an outflowing wind with fixed input energy and momentum will reach higher velocity at lower redshifts due to lower density of the IGM. However, this effect should be stronger between $z = 3.0$–$3.8$ than from $z = 3.8$–$4.7$, whereas the decrement in $W_{LIS}$ is much stronger from $z = 3.8$–$4.7$ (Figure 11). Furthermore, we measure a higher offset between the velocity centroid of Ly$\alpha$ emission and low-ionization absorption for $z > 4.1$ galaxies ($\Delta v = 660 \pm 80$) than for $z < 4.1$ ($\Delta v = 550 \pm 40$). Both measurements are consistent with the trend shown in Figure 10. Based on the trend of $W_{LIS}$ with $\Delta v$ seen at $z = 3$ (Shapley et al. 2003), we would then expect *stronger* $W_{LIS}$ at higher redshift. Kinematics are thus unable to explain the difference in $W_{LIS}$, at least with the information currently available. Data with higher spectral resolution and signal to noise are needed to fully address differences in the covering fraction and kinematics of neutral gas.

Another obvious potential cause of weaker $W_{LIS}$, or equivalently decreased $W_{Ly\alpha}$ at a fixed $W_{LIS}$, is the presence of neutral hydrogen with very low column density of heavy elements such as the IGM. Indeed, Laursen et al. (2011) examine the transmission of Ly$\alpha$ through the IGM and conclude that the Ly$\alpha$ line is increasingly attenuated between rest frame $1215\,\text{Å} < \lambda < 1216\,\text{Å}$ at higher redshifts ($2.5 < z < 6.5$). We can examine whether this affects the apparent evolution shown in Figure 11 by artificially attenuating the Ly$\alpha$ flux in the lower redshift composite. If the entire flux at $1215\,\text{Å} < \lambda < 1216\,\text{Å}$ is set to zero, then the equivalent width of Ly$\alpha$ decreases from $W_{Ly\alpha} = 15.4\,\text{Å}$ (as in Table 2) to $12.9\,\text{Å}$. Recognizing that the assumed systemic redshifts are imprecise, we set a firm limit on the maximum effect of IGM attenuation by setting the peak position of Ly$\alpha$ emission to zero over a range $\Delta\lambda = 1\,\text{Å}$. This results in $W_{Ly\alpha} = 10.2\,\text{Å}$, which we take as a lower limit of the flux that would be observed at higher redshifts. This limit is still consistent with the value $W_{Ly\alpha} = 12.2 \pm 3.7$ measured in the high-redshift composite, and hence we conclude that IGM transmission does not significantly affect the observed evolution of $W_{LIS}$. If the weaker $W_{LIS}$ is due to another source of neutral hydrogen with low column densities of heavy elements, then we would expect optically thin absorption line profiles. This could be directly tested as shown in Section 4.3.1, but the signal to noise of Si II $\lambda 1527$ in the high-redshift composite is too low to constrain the optical depth. We do see some evidence that the column density of neutral gas is lower at higher redshifts based on Ly$\alpha$ line profiles in the composite spectra, shown in Figure 12. The Ly$\alpha$ absorption trough at $\sim$1200–1215 Å is significantly weaker in the higher redshift composite. This absorption arises at least in part from damping wings of high column density gas with $N_{HI} \gtrsim 10^{20}\,\text{cm}^{-2}$ associated with the low-ionization metal absorption lines (e.g., Pettini et al. 2000, 2002). The higher redshift galaxies are therefore characterized by lower typical $N_{HI}$ or/and a lower covering factor of high column density gas. Higher signal-to-noise data at $z \simeq 5$ are required to determine whether this affects the optical depth of low-ionization metal transitions.

Weaker low-ionization lines could also be caused by a systematically higher ionization state at higher redshifts resulting in lower column densities of low-ionization gas. This would also explain the weaker damped Ly$\alpha$ absorption trough seen at higher redshifts (Figure 12). This scenario can be tested by measuring the equivalent widths of higher-ionization silicon transitions, in particular Si III $\lambda 1206$ and Si IV $\lambda\lambda 1393,1402$. We find that the Si IV lines are weaker at higher redshift by a factor of $0.68 \pm 0.25$ in $W_{Si IV \lambda\lambda 1393,1402}$, consistent with the decrement in $W_{Si II}$. We
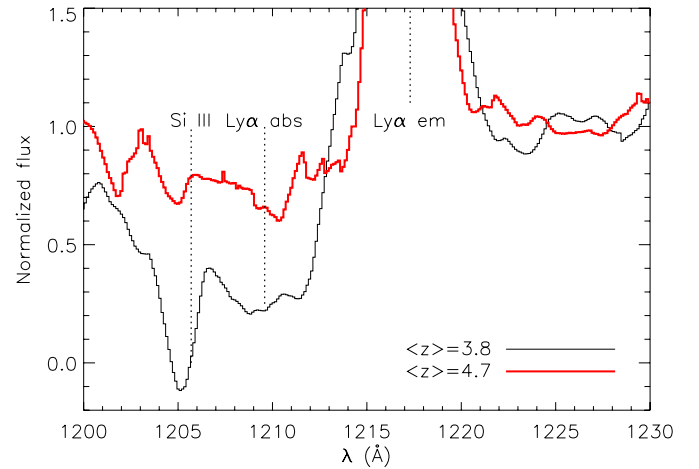


**Figure 12.** Composite spectra of LBGs showing the region around Ly$\alpha$ for the two redshift ranges described in Section 6. We show the position of Si III $\lambda 1206$ blueshifted by 200 km s$^{-1}$, Ly$\alpha$ emission redshifted by 400 km s$^{-1}$, and Ly$\alpha$ absorption blueshifted by 1500 km s$^{-1}$ where it is seen most prominently. The Ly$\alpha$ absorption trough is weaker in the higher redshift composite indicating a lower incidence of neutral gas with high column density. Si III absorption is also weaker in the higher redshift composite.

(A color version of this figure is available in the online journal.)

do not detect the Si III $\lambda 1206$ line in the high-redshift composite, with a $1\sigma$ upper limit of $W_{Si III} < 0.8$ times that of the lower redshift composite. Si III $\lambda 1206$ is marked in Figure 12 and is clearly stronger at lower redshift. We therefore find no evidence of a significant change in the ionization state of outflowing gas at higher redshifts.

A final possibility for lower column density of heavy elements is that Ly$\alpha$ is scattered by "cold streams" of nearly metal-free neutral gas, predicted by simulations to accrete onto galaxies at small radii and with increasing rates at higher redshift (e.g., Dekel et al. 2009; Faucher-Giguère et al. 2011). If they exist, then such streams could be identified as H I absorption systems with no corresponding absorption from heavy elements. Steidel et al. (2010) find little evidence for the presence of such streams around LBGs at $z = 2$–$3$. A similar study at higher redshift would be very interesting but also extremely challenging with current observational facilities.

Could the difference in $W_{LIS}$ with redshift be caused in part by a different physical extent of circumgalactic gas? In Section 4.3.2, we showed that fine-structure emission lines can be used to measure the amount of absorption taking place within the size of the spectroscopic aperture. This quantity does appear to change with redshift, in the sense that absorption takes place at a smaller characteristic radius in LBGs at higher redshift. The composite spectra of LBGs at $z = 4$ have weaker absorption lines and stronger fine-structure emission than the $z = 3$ composite of Shapley et al. (2003; Figure 4), in qualitative agreement with trends seen at $z = 3$ (Shapley et al. 2003; see their Figure 9). We have only a weak constraint on the redshift evolution at $z > 4$ due to limited signal to noise in the high-redshift composite. The ratio of total Si II fine-structure emission $W_{Si II*}$ in the high- and low-redshift composites is $1.1 \pm 0.5$ (taken as

$$\frac{W_{1265} + W_{1309} + W_{1533}}{W_{1260} + W_{1303} + W_{1527}}$$

with values given in Table 2), while the corresponding ratio of absorption line strength $W_{LIS}$ is $0.6 \pm 0.2$. The inferred

fraction of low-ionization absorption within the slit aperture is thus a factor of $1.8 \pm 1.0$ larger in the higher redshift sample, consistent with no evolution. Higher signal to noise is required to accurately constrain the spatial extent of low-ionization absorption at $z > 4$.

To summarize, we find weaker low-ionization absorption lines in LBGs at higher redshift with fixed $M_{UV}$. The difference in $W_{LIS}$ is not consistent with the trends observed for Ly$\alpha$ and various demographic properties examined in Section 5. We have discussed several possible causes for this discrepancy, including variation in the kinematics, covering fraction, optical depth, ionization state, and spatial extent of absorbing gas. The data show that the ionization state has no significant effect, but we are unable to conclusively address other possible causes. Spectra of galaxies at $z > 4$ with higher signal to noise are required to more accurately constrain the optical depth and spatial extent. Additionally, spectra of individual galaxies taken with higher spectral resolution will be required to independently determine the covering fraction and kinematic structure of absorbing gas.

### 6.1. Galaxy Evolution

We argue in Section 5 that Ly$\alpha$ equivalent width is determined primarily by the neutral CGM, which is correlated with various demographic galaxy properties (Figure 9). It is well established that these demographic properties vary with redshift and we expect $W_{Ly\alpha}$ to vary accordingly. Large photometric surveys have shown that LBGs at increasingly higher redshifts of $z > 3$ have lower luminosities (Bouwens et al. 2007, 2011a), bluer UV spectral slopes (Bouwens et al. 2009, 2011b), smaller stellar masses (Stark et al. 2009; González et al. 2011), and smaller sizes (Bouwens et al. 2004; Ferguson et al. 2004). This is in accordance with inside-out galaxy growth: galaxies increase in size and stellar mass as they evolve with time, while increasing metallicity and dust content reddens the ultraviolet continuum. Simultaneously, star formation drives large-scale outflows of gas which reach larger distances and are accelerated to larger velocities at later times (e.g., Murray et al. 2010). Galaxies which are more evolved (i.e., larger, more massive, and redder) should therefore have a CGM characterized by larger spatial extent, larger velocity range, and higher covering fraction of neutral gas. Observationally, this results in weaker $W_{Ly\alpha}$, stronger $W_{LIS}$, and relatively weaker fine-structure emission. These are precisely the trends observed at both $z = 3$ (Shapley et al. 2003) and $z = 4$ (this work).

### 6.2. Ly$\alpha$ in the Epoch of Reionization

We reiterate that LBGs at increasingly higher redshifts $z > 3$ have lower luminosities, bluer UV spectral slopes, smaller stellar masses, and smaller sizes. Notably, *all trends in the demographics of galaxies at higher redshift are correlated with stronger $W_{Ly\alpha}$ and weaker $W_{LIS}$* (Figure 9). We therefore expect typical galaxies at higher redshifts to have, on average, stronger Ly$\alpha$ emission. Earlier results from this survey confirm that strong Ly$\alpha$ emission is more frequent in galaxies at higher redshift (Paper I; Paper II). We find no evidence of this trend reversing. In fact, galaxies with extremely small size, low mass, and blue $\beta$ tend to be the strongest Ly$\alpha$ emitters (e.g., Erb et al. 2010). We do, however, expect the average Ly$\alpha$ emission strength to decrease significantly at increasing redshifts in the epoch of reionization due to neutral hydrogen in the IGM (e.g., Haiman & Spaans 1999).

We have devoted considerable discussion to the properties of Ly$\alpha$, in part because Ly$\alpha$ is of great interest as a tracer

of cosmic reionization. Several authors have now presented evidence that reionization was incomplete at $z \simeq 7$ based on a rapidly decreasing fraction of galaxies with strong Ly$\alpha$ emission at $z \gtrsim 6.5$ (Schenker et al. 2012; Ono et al. 2012; Pentericci et al. 2011). Although trends at $z = 3$–4 suggest that the galaxies observed by these authors should have a higher fraction of strong Ly$\alpha$ emission, we have presented evidence that the relation between $W_{Ly\alpha}$ and $W_{LIS}$ is systematically different at $z > 4$ (Figure 11). This implies a systematic difference in the spatial, kinematic, or optical depth structure of neutral circumgalactic gas compared to galaxies at lower redshift. The physical origin of this evolution and its effect on $W_{Ly\alpha}$ at $z > 4$ will need to be understood in order to fully interpret the results of Ly$\alpha$ surveys at higher redshifts in the context of reionization.

### 7. SUMMARY

The rest-frame ultraviolet spectra of star-forming galaxies contains a wealth of information about the properties of the circumgalactic medium. In this paper, we have presented an analysis of several features which trace the CGM with a focus on the properties of neutral gas. We find that the trends observed at lower redshift ($z = 3$; Shapley et al. 2003) also hold at $z = 4$ with approximately the same normalization (Figure 8). However, we find evidence for rapid evolution at $z > 4$ with lower $W_{LIS}$ at fixed $W_{Ly\alpha}$ and $M_{UV}$, suggesting a systematic difference in the spatial distribution, kinematics, ionization state, or optical depth of circumgalactic gas at higher redshifts. We determine that the ionization state is not responsible for the observed evolution, but are unable to distinguish between kinematics, covering fraction, optical depth, or the spatial extent of neutral gas as the likely cause. We are collecting additional spectra of LBGs at $z > 4$ with our ongoing survey, including high spectral resolution observations of bright lensed galaxies from which we can disentangle the kinematic profile and covering fraction of neutral gas. These data will allow us to address the precise magnitude and physical origin of evolution in circumgalactic gas properties.

As a final note, we emphasize that the neutral CGM is of great interest in the context of the reionization of the universe. Neutral gas in the circumgalactic medium absorbs ionizing radiation, thereby inhibiting the ability of galaxies to reionize the universe. The escape fraction of ionizing photons is one of the most important and uncertain factors in determining the contribution of star-forming galaxies to reionization (Robertson et al. 2010). We have shown that typical galaxies at higher redshift have weaker low-ionization absorption lines based on their demographic trends, and presented new evidence that absorption lines are systematically weaker at $z > 4$ even for fixed demographic properties. This is likely caused by a lower covering fraction and/or velocity range of neutral gas, and we will address the physical origin of this evolution with future data from our ongoing survey. Determining the redshift evolution of neutral gas covering fraction in LBGs will be of great interest for interpreting surveys of Ly$\alpha$ emission in the context of reionization and addressing the role of star-forming galaxies in reionizing the universe.

## REFERENCES

Bouwens, R. J., Illingworth, G. D., Blakeslee, J. P., Broadhurst, T. J., & Franx, M. 2004, ApJ, 611, L1
Bouwens, R. J., Illingworth, G. D., Franx, M., & Ford, H. 2007, ApJ, 670, 928
Bouwens, R. J., Illingworth, G. D., Franx, M., et al. 2009, ApJ, 705, 936
Bouwens, R. J., Illingworth, G. D., Oesch, P. A., et al. 2011a, ApJ, 737, 90
Bouwens, R. J., Illingworth, G. D., Oesch, P. A., et al. 2011b, arXiv:1109.0994
Brammer, G. B., Whitaker, K. E., van Dokkum, P. G., et al. 2011, ApJ, 739, 24
Davis, M., Faber, S. M., Newman, J., et al. 2003, Proc. SPIE, 4834, 161
Dekel, A., Birnboim, Y., Engel, G., et al. 2009, Nature, 457, 451
Eldridge, J. J., & Stanway, E. R. 2009, MNRAS, 400, 1019
Eldridge, J. J., & Stanway, E. R. 2012, MNRAS, 419, 479
Ellis, R. S. 2008, Saas-Fee Advanced Course 36: First Light in the Universe (Berlin: Springer), 259
Erb, D. K., Pettini, M., Shapley, A. E., et al. 2010, ApJ, 719, 1168
Faber, S. M., Phillips, A. C., Kibrick, R. I., et al. 2003, Proc. SPIE, 4841, 1657
Faucher-Giguère, C.-A., Kereš, D., & Ma, C.-P. 2011, MNRAS, 417, 2982
Ferguson, H. C., Dickinson, M., Giavalisco, M., et al. 2004, ApJ, 600, L107
Forero-Romero, J. E., Yepes, G., Gottloeber, S., & Prada, F. 2012, MNRAS, 419, 952
Giavalisco, M., Ferguson, H. C., Koekemoer, A. M., et al. 2004, ApJ, 600, L93
González, V., Labbé, I., Bouwens, R. J., et al. 2011, ApJ, 735, L34
Grogin, N. A., Kocevski, D. D., Faber, S. M., et al. 2011, ApJS, 197, 35
Haiman, Z., & Spaans, M. 1999, ApJ, 518, 138
Heckman, T. M. 2002, in ASP Conf. Ser. 254, Extragalactic Gas at Low Redshift, ed. J. S. Mulchaey & J. Stocke (San Francisco, CA: ASP), 292
Hopkins, A. M., & Beacom, J. F. 2006, ApJ, 651, 142
Kobulnicky, H. A., & Skillman, E. D. 1998, ApJ, 497, 601
Koekemoer, A. M., Faber, S. M., Ferguson, H. C., et al. 2011, ApJS, 197, 36
Kroupa, P. 2002, Science, 295, 82
Laursen, P., Sommer-Larsen, J., & Razoumov, A. O. 2011, ApJ, 728, 52
Maiolino, R., Nagao, T., Grazian, A., et al. 2008, A&A, 488, 463
Masters, D., & Capak, P. 2011, PASP, 123, 638
Murray, N., Quataert, E., & Thompson, T. A. 2010, ApJ, 709, 191
Oke, J. B. 1974, ApJS, 27, 21
Ono, Y., Ouchi, M., Mobasher, B., et al. 2012, ApJ, 744, 83
Ouchi, M., Shimasaku, K., Akiyama, M., et al. 2008, ApJS, 176, 301
Pentericci, L., Fontana, A., Vanzella, E., et al. 2011, ApJ, 743, 132
Pettini, M., Rix, S. A., Steidel, C. C., et al. 2002, ApJ, 569, 742
Pettini, M., Steidel, C. C., Adelberger, K. L., Dickinson, M., & Giavalisco, M. 2000, ApJ, 528, 96
Quider, A. M., Pettini, M., Shapley, A. E., & Steidel, C. C. 2009, MNRAS, 398, 1263
Quider, A. M., Shapley, A. E., Pettini, M., Steidel, C. C., & Stark, D. P. 2010, MNRAS, 402, 1467
Reddy, N. A., & Steidel, C. C. 2009, ApJ, 692, 778
Robertson, B. E., Ellis, R. S., Dunlop, J. S., McLure, R. J., & Stark, D. P. 2010, Nature, 468, 49
Schenker, M. A., Stark, D. P., Ellis, R. S., et al. 2012, ApJ, 744, 179
Shapley, A. E. 2011, ARA&A, 49, 525
Shapley, A. E., Steidel, C. C., Adelberger, K. L., et al. 2001, ApJ, 562, 95
Shapley, A. E., Steidel, C. C., Pettini, M., & Adelberger, K. L. 2003, ApJ, 588, 65
Stark, D. P., Ellis, R. S., Bunker, A., et al. 2009, ApJ, 697, 1493
Stark, D. P., Ellis, R. S., Chiu, K., Ouchi, M., & Bunker, A. 2010, MNRAS, 408, 1628
Stark, D. P., Ellis, R. S., & Ouchi, M. 2011, ApJ, 728, L2
Steidel, C. C., Adelberger, K. L., Shapley, A. E., et al. 2003, ApJ, 592, 728
Steidel, C. C., Bogosavljević, M., Shapley, A. E., et al. 2011, ApJ, 736, 160
Steidel, C. C., Erb, D. K., Shapley, A. E., et al. 2010, ApJ, 717, 289
Vanzella, E., Cristiani, S., Dickinson, M., et al. 2005, A&A, 434, 53
Vanzella, E., Cristiani, S., Dickinson, M., et al. 2006, A&A, 454, 423
Vanzella, E., Cristiani, S., Dickinson, M., et al. 2008, A&A, 478, 83
Vanzella, E., Giavalisco, M., Dickinson, M., et al. 2009, ApJ, 695, 1163
Wang, W.-H., Cowie, L. L., Barger, A. J., Keenan, R. C., & Ting, H.-C. 2010, ApJS, 187, 251
Wardlow, J. L., Smail, I., Coppin, K. E. K., et al. 2011, MNRAS, 415, 1479
Weiner, B. J., Coil, A. L., Prochaska, J. X., et al. 2009, ApJ, 692, 187